

# Langevin and Navier-Stokes Simulations of Three-Dimensional Protoplasmic Streaming and a Nontrivial Effect of Boundary Fluid Circulation

Shuta Noro <sup>1</sup>, Satoshi Hongo <sup>1</sup>, Shinichiro Nagahiro <sup>1</sup>, Hisatoshi Ikai <sup>1</sup>, Hiroshi Koibuchi <sup>2,\*</sup>, Madoka Nakayama <sup>3</sup>, Tetsuya Uchimoto <sup>4,5</sup>, and Gildas Diguët <sup>6</sup>

<sup>1</sup> *National Institute of Technology (KOSEN),  
Sendai College, 48 Nodayama, Medeshima-Shiote,  
Natori-shi, Miyagi 981-1239, Japan*

<sup>2</sup> *National Institute of Technology (KOSEN), Ibaraki College,  
866 Nakane, Hitachinaka, Ibaraki 312-8508, Japan*

<sup>3</sup> *Research Center of Mathematics for Social Creativity,  
Research Institute for Electronic Science,  
Hokkaido University, Sapporo, Japan*

<sup>4</sup> *Institute of Fluid Science (IFS), Tohoku University,  
2-1-1 Katahira, Aoba-ku Sendai 980-8577, Japan*

<sup>5</sup> *ELyTMax, CNRS-Universite de Lyon-Tohoku University,  
2-1-1 Katahira, Aoba-ku Sendai 980-8577, Japan*

<sup>6</sup> *Micro System Integration Center, Tohoku University,  
6-6-01 Aramaki-Aza-Aoba, Aoba-ku Sendai 980-8579, Japan*

## Abstract

In this paper, we report numerical results obtained using Langevin Navier-Stokes (LNS) simulations of the velocity distribution of three-dimensional (3D) protoplasmic streaming. Experimentally observed and reported peaks of the velocity distribution in plant cells, such as those of *Nitella flexilis*, were recently reproduced by our group with LNS simulations. However, these simulations are limited to Couette flow, which is a simplified and two-dimensional protoplasmic streaming phenomenon. To reproduce the peaks in natural 3D flows, the simulations should be extended to three dimensions. This paper describes LNS simulations on 3D cylinders discretized by regular cubes in which fluid particles are activated by boundary velocities of parallel and nonparallel to the longitudinal direction and a random Brownian force with strength  $D$ . We find that for finite  $D$ , the velocity distribution  $h(V)$ ,  $V = |\vec{V}|$ , has two different peaks at a small non-zero  $V$  and a finite  $V$ , and the quantity  $h(V_z)$  for  $|V_z|$  along the longitudinal direction is also nontrivially influenced by Brownian motion. Moreover, we study the effects of Brownian motion on biological material mixing and find that the mixing enhanced by the nonparallel circular motion is further improved by Brownian motion.

---

\* koibuchi@ibaraki-ct.ac.jp; koibuchih@gmail.com

## I. INTRODUCTION

The diameter of plant cells, such as those of *Nitella flexilis*, may be as high as 1 (mm) in water, and the flow in these cells, termed protoplasmic streaming, has recently attracted considerable interest from researchers in the biological and agricultural fields [1–3]. Figures 1(a) and (b) show an optical image of a plant in water and illustrate the streaming and its direction inside a cell, respectively.

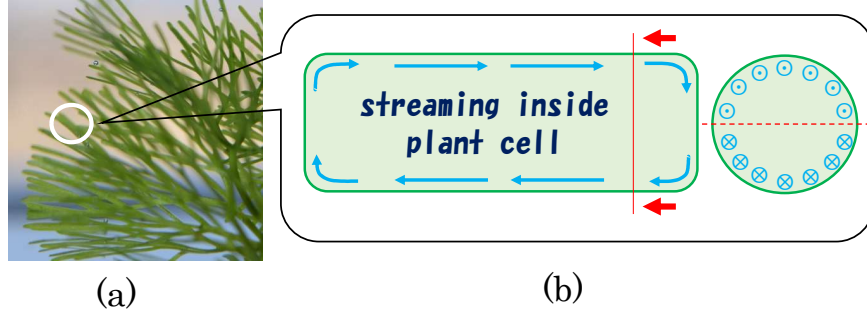


FIG. 1. (a) Plant in water (image obtained using an optical camera), (b) illustration of the boundary flow that causes streaming inside cells, and the flow directions at the boundary region in a cell section.

The flow in plant cells is driven by a so-called molecular motor, where a myosin molecule moves along actin filaments. Hence, the flow activation mechanism is the same as that in animal cells [4–7]. Recently, Tominaga et al. reported that the size of a plant depends on the streaming velocity, which implies that the velocity of myosin molecules determines the plant size [3]. To date, protoplasmic streaming has been extensively studied using experimental and theoretical techniques, including fluid dynamical simulations [8–13].

Kamiya and Kuroda first measured the flow velocity  $V_z$  ( $\mu\text{m/s}$ ) along the longitudinal direction of a cell using an optical microscope ( $V_z$  in Fig. 2(a)) [14, 15]. The corresponding physical quantities have also been reported; the kinematic viscosity is approximately 100 times larger than that of water [16–18]. In Ref. [19], Pickard reported further observations of the streaming including the angular and radial variations of the velocity with theoretical analyses. The flow direction along the side of the cell boundary is not always parallel to the longitudinal axis; rather, it is twisted, forming a so-called indifferent zone (Fig. 2(a)). The angle  $\phi$  of the indifferent zone of *Nitella axilliformis* Imahori in Fig. 2(b) is approximated

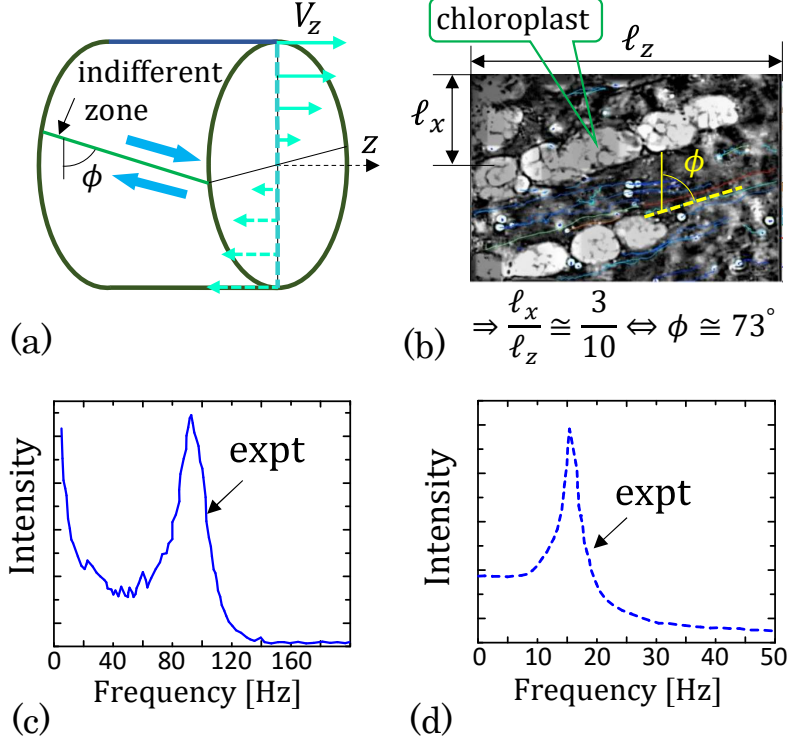


FIG. 2. (a) Flow velocity  $\vec{V}$  inside a cell, (b) photograph of *Nitella axilliformis Imahori* taken at the inner wall of an internodal cell [20], (c) scattered light intensity vs. Doppler shift frequency obtained using a laser-light scattering technique, where the peak at 93 Hz corresponds to a velocity of 72 ( $\mu\text{m/s}$ ) [22], and (d) another reported scattered-light intensity in [23]. The Doppler shift frequency depends on the scattering angle. The solid line in (a) denotes the indifferent zone, where two opposite boundary velocities contact each other. The angle  $\phi$  of the indifferent zone of *Nitella axilliformis Imahori* is estimated to be approximately  $\phi = 73^\circ$  from  $\ell_x/\ell_z \simeq 3/10$  in (b), where the  $z$  direction is parallel to the longitudinal axis of the cell.

to be  $\phi = 73^\circ$  [20]. Subsequently, using magnetic resonance velocimetry on cylinder cross-sections, Goldstein et al. measured the velocity and reported the positional dependence of several different lines on the cross-sections [10]. They also theoretically studied the flow field by combining the Stokes equation or Navier-Stokes (NS) equation for low Reynolds numbers and an advection-diffusion equation for a new variable concentration. Their results agreed well with the experimental results and they reported that biological material mixing is enhanced by the rotational boundary flow [8–11].

Approximately 25 years after Kamiya and Kuroda's measurements, Mustacich and Ware

observed streaming using a laser-light scattering technique [21–24]. They reported that the scattered light spectra show two different peaks at  $V \rightarrow 0$  and  $V \neq 0$  (Fig. 2(c)) and a single peak at  $V \neq 0$  (Fig. 2(d)). The peak velocity at  $V \neq 0$  is the streaming velocity. We should note that the Brownian motion influences fluid particles not only in the  $V \rightarrow 0$  limit but also in all velocity ranges. This is the reason for the appearance of velocities in a range larger than the peak in the velocity distribution.

Recently, the peaks were numerically reproduced in Refs. [25, 26] by simplifying the three-dimensional (3D) streaming to two-dimensional (2D) Couette flow and using the Langevin Navier-Stokes (LNS) equation, which includes a random Brownian force term as an activation force [27]. However, the 3D streaming nature, such as the circulation at the cell boundary, was modified to be parallel to the longitudinal direction in the 2D simulations. Therefore, 3D simulations are preferable to better understand the streaming.

At present, there is no report on 3D simulations that include the effects of the Brownian motion of fluids on protoplasmic streaming. Here, we should comment on the basic assumption imposed on the streaming. The fluid flow inside the vacuole of a plant cell includes many biological materials, so these materials scatter laser light [21–24]. However, the size of the biological materials is not uniform and is expected to range from the size of molecules ( $\simeq 10$  (nm)) to the size of the cytoplasm ( $\simeq 5$  ( $\mu$ m)), and the density of mass is comparable with that of water. Therefore, we simply regard the streaming as a fluid flow described by the NS equation rather than a colloidal suspension, which is described by the equations of motion of particles such as those in Brownian Dynamics [27].

In this study, we model streaming using a 3D LNS simulation technique for variable velocities and pressures inside the cylindrical volume and at its boundary. The LNS equation introduced in this paper is included in the framework of the LNS equation introduced statistically mechanically by Landau and Lifschitz implying that only the mean values of physical quantities are meaningful as observable quantities [28].

As mentioned above, colloidal suspensions in fluids are simulated using the so-called Stokesian Dynamics or Brownian Dynamics [29–31]. In this technique, the hydrodynamic interactions of particles as well as the interactions between particles are implemented. The notion of fluid particles was introduced as Dissipation Particle Dynamics (DPD) to simulate fluids with thermal fluctuations [32–34]. Our LNS equation technique is close to DPD except that the fluid particles are treated as rigid in DPD. Thermal fluid fluctuations are also studied

using the so-called Immersed Boundary Method for biological systems, in which the external forces including the Brownian force act on both the fluid and the immersed boundary [35–37]. Our LNS simulation technique is also close to but slightly different from this Immersed Boundary Method.

In the case of the lattice Boltzmann method (LBM), velocity distribution functions are simulated, and physical quantities such as the velocity and pressure are calculated using these functions [38–42]. Therefore, the variables solved in the LBM are different from those in the NS equation, although the NS equation can be derived from the LBM equations under certain conditions [42]. Moreover, the velocity distribution functions in the LBM are considered to be defined for a lump of fluid particles. In this sense, the LBM also shares a particle simulation scheme. A Langevin equation is used as a numerical technique in particle physics for functions on a lattice [43–45], so we consider that the Brownian motions can be combined with the NS equation for fluids [46]. Thus, LNS simulations partly include a particle simulation scheme.

The primary objectives of our study are to find two different peaks in the velocity distribution corresponding to the experimentally observed velocities and determine whether the circulation of the particles at the cell boundary has a nontrivial effect on the protoplasmic streaming. We find that the mean values of the velocities inside the cell are increased by the rotating circulation even without Brownian motion, and the maximum velocity becomes larger than the case of parallel circulation under the presence of Brownian motion. This maximum speed increment implies that random Brownian motion plays an essential role in enhancing mixing. In this sense, the result also shows that the experimentally observed peaks and the mixing enhancement are connected to the microscopic origin.

## II. METHODS

### A. Langevin Navier–Stokes equation and discrete equation

The LNS equation is given by a set of coupled equations for the velocity  $\vec{V} = (V_x, V_y, V_z)(\text{m/s})$  and pressure  $p(\text{Pa})$ :

$$\begin{aligned} \frac{\partial \vec{V}}{\partial t} &= - \left( \vec{V} \cdot \nabla \right) \vec{V} - \rho^{-1} \nabla p + \nu \Delta \vec{V} + \vec{\eta}, \\ \nabla \cdot \vec{V} &= 0, \end{aligned} \tag{1}$$

where  $\rho(\text{kg/m}^3)$  and  $\nu(\text{m}^2/\text{s})$  denote the fluid density and kinematic viscosity, respectively [25, 26]. The final term  $\vec{\eta}(\text{m/s}^2)$  on the right-hand side of the first equation corresponds to the random Brownian force per unit density. Because of this random force, the variables  $\vec{V}$  and  $p$  fluctuate very rapidly in a small distance, and the mean value  $\langle \vec{V} \rangle$  can be obtained as an observable physical quantity, as mentioned in the introduction. The meaning of the symbol  $\langle * \rangle$  is introduced in the following subsection from the simulation viewpoint.

The velocity  $\vec{V}$  and pressure  $p$  variables are used in Eq. (1), which is different from the LNS equation for the flow function  $\psi$  and vorticity  $\omega$  in Ref. [25], where the condition  $\nabla \cdot \vec{V} = 0$  is exactly satisfied for all  $t$ . In contrast, this divergenceless condition is not always satisfied in the time evolution of Eq. (1) even if it is satisfied in the initial configuration. The original marker and cell (MAC) method is a simple technique to resolve this problem [47]; however,  $\nabla \cdot \vec{V} = 0$  is not always satisfied even at the convergent solution satisfying  $\partial \vec{V} / \partial t = 0$ ; hence, the well-known simplified MAC (SMAC) method is used in this study.

To solve Eq. (1), we impose the steady state condition

$$\frac{\partial \vec{V}}{\partial t} = 0. \quad (2)$$

To obtain  $\vec{V}$  satisfying this condition, we numerically solve the following discrete equation with time step  $\Delta t$ :

$$\vec{V}(t + \Delta t) = \vec{V}(t) + \Delta t \left[ \left( -\vec{V} \cdot \nabla \right) \vec{V}(t) - \rho^{-1} \nabla p(t + \Delta t) + \nu \Delta \vec{V}(t) \right] + \sqrt{2D\Delta t} \vec{g}, \quad (3)$$

where we use the same symbol  $t$  for the discrete time in this equation as for the real time  $t$  in the original LNS equation in Eq. (1). This difference in time and detailed information of the SMAC method to obtain the solution to Eq. (3) under the condition in Eq. (2) is shown in Appendix A.

## B. Lattices for simulations and boundary conditions

We show the details of the lattice construction for a cylindrical streaming domain in plant cells. The actual cell surface is soft and expected to bend and fluctuate. However, it is relatively rigid compared with the surface of animal cells [55], so we assume that the cylinder surface is rigid for simplicity. Thus, for the computational domain, we assume a 3D cylinder of radius  $R$  and length  $L$  (Fig. 3). The unit length is fixed to the lattice spacing

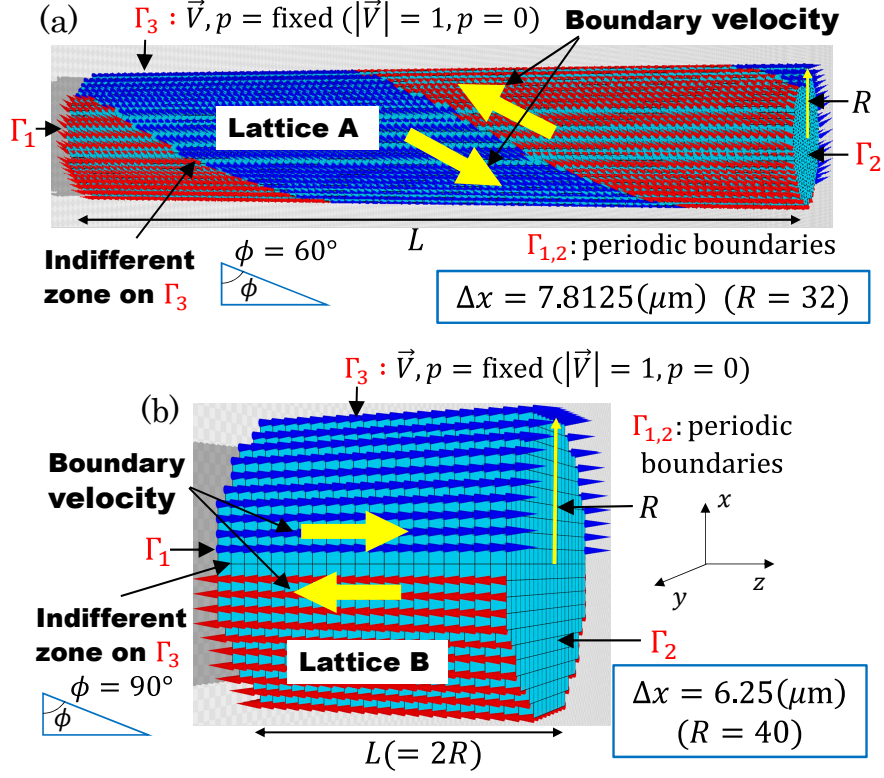


FIG. 3. 3D cylindrical computational domains of (a) lattice A and (b) lattice B for streaming. The arrows in (a) and (b) indicate the directions of the boundary velocity that activates the streaming inside the cylinder, and the small cones represent the velocity directions. The length  $L$  of the cylinder is determined such that the indifferent zone rotates once around the boundary  $\Gamma_3$ :  $L = 2\pi(R + 1) \tan \phi$  (with the unit of the lattice spacing  $\Delta x$ ); consequently, the velocities and pressures on  $\Gamma_1$  and  $\Gamma_2$  are connected by the periodic boundary condition on lattice A.  $L$  is fixed to  $L = 2R$  on lattice B. For a clear visualization of the cones, the diameters of the cylinders in (a)  $R = 8$  and (b)  $R = 10$  are four times smaller than those (a)  $R = 32$  and (b)  $R = 40$  used for the simulations. The velocity  $\vec{V}$  and pressure  $p$  are fixed to  $|\vec{V}| = 1$  and  $p = 0$  in the simulation units on  $\Gamma_3$  as the boundary conditions for both lattices A and B.

$\Delta x$ , which is assumed to be  $\Delta x = 1$  in this and subsequent subsections. Therefore,  $R\Delta x$  and  $L\Delta x$  are written as  $R$  and  $L$  for simplicity. The lattice spacing  $\Delta x$  is restored for the physical or simulation unit in the following section. The regions indicated by the symbols  $\Gamma_i$ , ( $i=1, 2, 3$ ) in the figure denote the boundary surfaces.

The fluid is activated by the molecular motors on the surface  $\Gamma_3$ , and the fluid particles



are dragged along the boundary, as indicated by the two large arrows in Fig. 3. The contact line along which two different velocities coexist is called the indifferent zone and divides  $\Gamma_3$  into two domains. The angle of the zone is fixed to  $\pi/3$  (or  $60^\circ$ ) on lattice A, and the volume of the computational domain depends on this angle. An angle of  $60^\circ$  is assumed, which is smaller than the actual angle in plant cells, as shown in Fig. 2(b), to save computational time. The length  $L$  of the cylinder is fixed such that the indifferent zone rotates once around  $\Gamma_3$ . Therefore, the boundaries  $\Gamma_1$  and  $\Gamma_2$  are connected by a periodic boundary condition such that the velocities  $\vec{V}$  and pressures  $p$  on  $\Gamma_1$  and  $\Gamma_2$  are nearest neighbors to each other. The boundary velocity  $\vec{V}$  ( $|\vec{V}| = 1$  in the simulation units: Appendix B) on  $\Gamma_3$  on lattice A is fixed to be a unit tangential vector, and the orientation in one domain is opposite to that in the other, as shown in Fig. 3(a). The tangential vectors are characterized by  $|V_z| = \sin \phi$  ( $\phi = 60^\circ$ ), where  $V_z$  is the  $z$ -component of  $\vec{V}$ . On lattice B, the boundary velocity is fixed to  $|\vec{V}| = |V_z| = 1$ . Another boundary condition is  $p = 0$  for all points on  $\Gamma_3$  of both lattices A and B. From the computational viewpoint,  $p$  should be fixed somewhere in the computational domain or at the boundary. Since no difference is expected at the points on  $\Gamma_3$ , we impose this condition on  $p$ .

To explain the lattice structure, we show a cross-section of the cylinder (Fig. 4(a)). The building block is a regular cube with side length  $\Delta x$ , which is the lattice spacing. Therefore, the boundary shape is not a circle. Let  $r$  be the distance of a vertex from the center of the cross-section. The vertices in region  $R-1 < r < R+1$  form the boundary, whereas those in region  $r < R-1$  are the internal points, where  $R$  is the radius of the horizontal and vertical lines passing through the center of the cross-section.

The notion of a lump of fluid particles is based on coarse-graining, which is used as an established notion in polymer physics [48, 49]. This notion is also assumed in membrane simulations [50, 51], where a lump of lipids is considered to be particles diffusing like a fluid over a surface. The notion of coarse-graining is always assumed in lattice simulations in many fields including the physics of forces between elementary particles [52], where the temperature is not always limited to room temperature. As described in the Introduction, the LBM utilizes this notion for fluid particles.

Thus, we express lumps of fluid particles simply as “fluid particles” in this paper. Figures 4(b), (c) and (d) show images of fluid particle lumps. The dashed circles express the domains. The size should not be overlapped, and it should also be larger than the size of a water

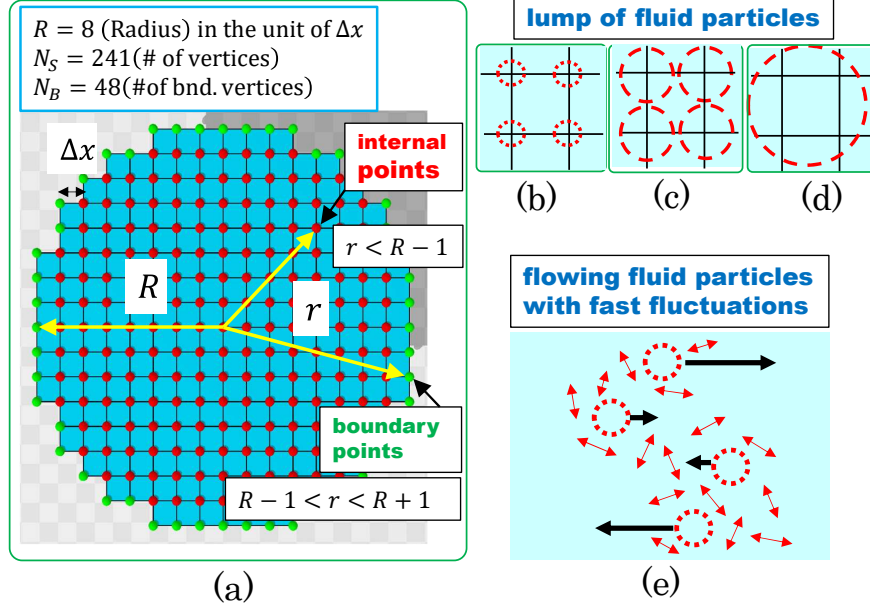


FIG. 4. (a) Cross-section of a cylindrical lattice of size  $R=8$ , which is 4 to 5 times smaller than the  $R=32$  and  $R=40$  of the lattices for the simulations. The total number of vertices is  $N_S=241$ , which includes  $N_B=48$  boundary vertices. The radius  $r$  of the boundary vertices, at which the velocity  $\vec{V}$  and pressure  $p$  are fixed, is given by  $R-1 < r < R+1$ , and the  $r$  value of the internal vertices is given by  $r < R-1$ . (b), (c), (d) Images of fluid particles drawn by dashed circles, of which the size is (b) less than, (c) comparable to, and (d) larger than the lattice spacing  $\Delta x$ . (e) Image of flowing fluid particles with observable velocities ( $\rightarrow$ ) and rapid and small-distance fluctuations ( $\leftrightarrow$ ).

molecule and less than approximately  $100(\mu\text{m})$ , which is the upper limit of the thermally-fluctuating particle size at room temperature. The velocity  $\vec{V}$  is only defined at the mesh points (Fig. 4(a)) and accelerated by random forces at these mesh points. Therefore, the velocity of a fluid particle larger than the mesh size is activated at many points by random forces, and its position can be determined by their mean value. However, the particle boundaries in fluids are not calculated and are treated as physically non-observable in our scheme, and hence, only the velocities at mesh points are used to understand the flow field. Fluctuations are considered isotropic, and therefore, the mean velocity of the fluctuations is zero. For this reason, the observable protoplasmic steaming velocity, as illustrated in Fig. 2(a), is determined by the boundary flows. Figure 4(e) shows an image of fluid particles

moving with isotropic and rapid fluctuations. Fluid dynamical forces other than the random force also change the velocities on the mesh points as in the standard treatment of the NS equations.

In Table I, we summarize the geometries of lattices A and B. On the surface of lattice A, the angle  $\phi$  between the indifferent zone and the vertical direction is set to  $\phi = 60^\circ$  to examine the effects of the velocity rotation on the boundary  $\Gamma_3$ , while it is assumed to be  $\phi = 90^\circ$  on lattice B (Fig. 3(a) and (b)).

The size of both lattices is relatively small due to the stochastic nature of the model because many convergent configurations are necessary to obtain the mean values of physical quantities. The mean value of the physical quantity  $\langle Q \rangle$  is obtained by

$$\langle Q \rangle = (1/n_s) \sum_{i=1}^{n_s} Q_i, \quad (3)$$

where  $Q_i$  denotes the  $i$ -th convergent configuration corresponding to the  $i$ -th Gaussian random force  $\vec{\eta}(t)$ . The symbol  $n_s$  is the total number of convergent configurations, and  $n_s = 1000$  for the calculation of  $\vec{V}(r, \theta)$ , which will be shown in the following subsection, for all  $D$  except  $D = 0$ . For  $D = 0$ ,  $n_s$  should be  $n_s = 1$  because no Gaussian random number is assumed in this case. For simplicity, the brackets  $\langle \cdot \rangle$  are not used for the mean values in this paper. If the lattice size is too small, then the flows at the boundary  $\Gamma_3$  in Fig. 3(a) and (b) are too strong for internal flows. In this case, vortex flows such as those observed in the 2D Couette flow in Ref. [25] and the peaks in the velocity distribution as shown in Fig. 2(c) are not expected. However, if peaks are observed in the velocity distribution, this

TABLE I. Two different lattice geometries for the simulations. The ratio  $L/R$  is approximately  $L/R \simeq 11.2$  on lattice A, while it is exactly  $L/R = 2$  on lattice B, where  $L$  is the cylinder length and  $R$  is the radius with the unit of lattice spacing  $\Delta x (= 1)$  (Fig. 3(a) and (b)). The reason for the difference in  $L/R$  on lattices A and B is discussed in the caption of Fig. 3.

| Lattice | $\phi$     | $R$ | $L$ | Internal<br>vertices | Boundary<br>vertices |
|---------|------------|-----|-----|----------------------|----------------------|
| A       | $60^\circ$ | 32  | 359 | 1,153,800            | 66,240               |
| B       | $90^\circ$ | 40  | 80  | 406,053              | 18,468               |

observation implies that the flows are influenced by Brownian motion and the lattice size is sufficient for the present purpose.

Here, we emphasize that the numerical technique for obtaining the physical quantities in this study and in Refs. [25, 26] is based on Eq. (3). This calculation technique is used to obtain the canonical ensemble averages of physical quantities in statistical mechanical simulations such as the Metropolis Monte Carlo simulation technique [53, 54]. In those Monte Carlo simulations, all physical quantities are obtained using the mean value calculation in Eq. (3), where all  $Q_i$  are calculated from the variables distributed according to a Boltzmann distribution  $\exp(-S/k_B T)$  with an assumed Hamiltonian weight  $S$ . Our technique for solving the LNS equation shares this property due to the general framework of the statistical mechanical treatment of the fluid dynamical fluctuations implemented as a Brownian motion of fluids in the equation of Ref. [28], as mentioned above. The aim of the LNS equation is not to find the time evolution of the fluid flow in long time scale but simply to obtain the equilibrium velocity configuration under thermal fluctuations.

### C. Normalized velocity distributions $h(V)$ , $h(V_z)$ and the radial dependence of $V_z$

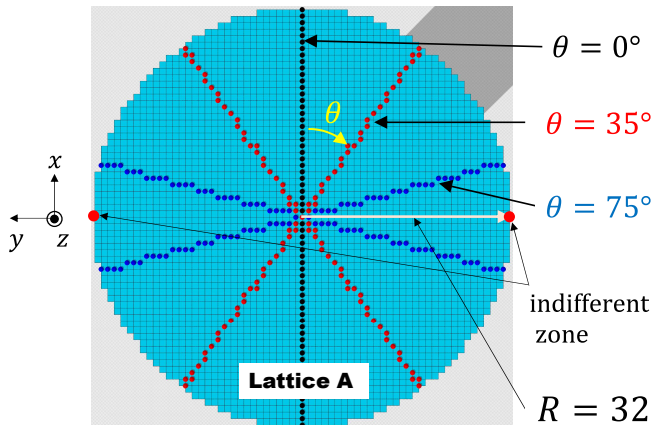


FIG. 5. Lattice points along the lines of three different angles  $\theta$  for the calculation of  $V_z(r, \theta)$ . The line at  $\theta = 0^\circ$  is a vertical line along the  $x$  axis, while those at  $\theta = 35^\circ$  and  $\theta = 75^\circ$  are two symmetric lines due to the reflection symmetry  $\theta \rightarrow -\theta$ . The lattice section corresponds to lattice A, the radius of which is given by  $R=32$  with the unit of lattice spacing  $\Delta x (=1)$ .

The dependence of  $V_z(r, \theta)$  on  $r$  is numerically measured along the lines in Fig. 5 with

angles  $\theta = 0^\circ, 35^\circ, 75^\circ$  on the cross-section at  $z = L/2$  at the middle point of the cylinder. These angles are almost the same as those assumed in Ref. [10]. Only a single cross-section is used for the numerical measurements of  $V_z(r, \theta)$  on lattice A because the boundary velocities are rotating, and there is no equivalent cross-section along the longitudinal direction of the cylinder, although the cross-sections at  $z = 0$  and  $z = L$  are almost equivalent due to the periodicity of the circulation (Fig. 3(a)). In the case of lattice B, all of cross-sections are equivalent; however, we also use the cross-section at  $z = L/2$  to numerically measure  $V_z(r, \theta)$ , as in the case of lattice A.

The experimentally observed laser-light scattering intensity in Fig. 2(c) is considered to correspond to the velocity distribution  $h(V_z)$ , which has no  $\theta$  dependence. Therefore, we calculate  $h(V_z)$  and  $h(V)$  on all cross-sections, while the radial  $r$  dependence of  $V_z(r, \theta)$  for three different  $\theta$  angles is calculated on the cross-section at the center of the longitudinal direction of lattice as mentioned above. Detailed information on the  $h(V)$  and  $h(V_z)$  calculation technique is shown in Appendix C.

#### D. Input parameters

The physical parameters that characterize protoplasmic streaming are the density  $\rho_e(\text{kg/m}^3)$ , kinematic viscosity  $\nu_e(\text{m}^2/\text{s})$ , boundary velocity  $V_e(\text{m/s})$ , and diameter of the cell  $d_e(\text{m})$ , which are given in Table II. These values are given in Refs. [14–18] and are the

TABLE II. Physical parameters  $\nu_e$ ,  $V_e$ , and  $d_e$  corresponding to the protoplasmic streaming in plant cells, expressed in physical units. The estimated Reynolds number is  $Re = V_e d_e / \nu_e = 2.5 \times 10^{-4}$ .

| $\rho_e(\text{kg/m}^3)$ | $\nu_e(\text{m}^2/\text{s})$ | $V_e(\mu\text{m/s})$ | $d_e(\mu\text{m})$ |
|-------------------------|------------------------------|----------------------|--------------------|
| $1 \times 10^3$         | $1 \times 10^{-4}$           | 50                   | 500                |

same as those assumed in the 2D LNS simulations in Refs. [25, 26]. Note that the boundary velocity  $V_e$  is very small, implying that the first term or the advection term in the right hand side of Eq. (1) is negligibly small. In this sense, the LNS equation in Eq. (1) or (3) can be called a Langevin Stokes equation, and moreover, the fact that the advection term is negligible implies that analyses reported in Refs. [8, 9] are suitable for protoplasmic

streaming. The Reynolds number of the streaming can be estimated with the parameters in Table II such that  $R_e = V_e d_e / \nu_e = 2.5 \times 10^{-4}$ .

Using the factors  $\alpha, \beta$  and  $\lambda$  for the unit change (see Appendix B), we obtain the parameters in Table III in the simulation units, which are used in the simulations in this study. The strength  $D$  of the Brownian motion is varied in the simulations because this is nec-

TABLE III. Parameters assumed in the simulations; these values are given in the simulation units. The lattice spacing  $\Delta x (= d_e / n_X)$  is given by  $\Delta x = 7.8125(\mu\text{m})$  (lattice A:  $n_X = 64$ ) and  $\Delta x = 6.25(\mu\text{m})$  (lattice B:  $n_X = 80$ ) in the physical unit, where  $d_e = 500(\mu\text{m})$ .

| Lattice | $\rho_0 [\frac{\lambda\text{kg}}{(\alpha\text{m})^3}]$ | $\nu_0 [\frac{(\alpha\text{m})^2}{\beta\text{s}}]$ | $V_0 [\frac{\alpha\text{m}}{\beta\text{s}}]$ | $\Delta x_0 [\alpha\text{m}]$ | $\Delta t_0 [\beta\text{s}]$ |
|---------|--|--|--|-------------------------------|------------------------------|
| A       | $1 \times 10^{-3}$                                     | $1 \times 10^6$                                    | 1  | 3.90625                       | $5 \times 10^{-7}$           |
| B       | $1 \times 10^{-3}$                                     | $1 \times 10^6$                                    | 1  | 3.125                         | $5 \times 10^{-7}$           |

essary to observe the dependence of the velocity distributions on the physical parameters  $\nu_e, V_e$ , and  $d_e$  [25, 26]. Thermal fluctuations are expected to be dependent on these physical parameters, and therefore, we expect that  $D$  depends on them. Note that  $D$  without units, which is used in the following section, is expressed with the simulation units  $((\alpha\text{m})^2/(\beta\text{s})^3)$  (Appendix B).

We consider that  $D$  is the only parameter that can be varied in the simulations. Indeed, the target phenomenon is characterized by  $(\rho_e, \nu_e, V_e, d_e)$  in Table II, and the corresponding parameters  $(\rho_0, \nu_0, V_0, \Delta x_0)$  in the simulation units are determined as in Table III. Therefore, the remaining parameters  $\Delta t_0$  and  $D_0$  are varied to find the velocity distributions  $h(V_z)$  and  $h(V)$ . Thus, if we fix  $\Delta t_0$  to some value, then the variable parameter is only  $D_0$ , which is written as  $D$  for the presentation of simulation results in the following section. In this sense, the 3D LNS simulations with the variable parameter  $D$  are similar to the dimensionless approach in the standard NS simulations, where the Reynolds number  $R_e$  is the only variable parameter. We note that varying  $D$  implies that the target system also changes. Therefore, we should find a  $D$  suitable to the thermal fluctuations of the target system by comparing the simulated  $h(V_z)$  with the experimentally observed and reported  $h(V_z)$ . Once a  $D_{\text{sim}}$  or a range of  $D_{\text{sim}}$  that is suitable to the system under consideration is found, a further variation of  $D$  from this  $D_{\text{sim}}$  implies a variation in the system. The viscosity  $\nu_e$  depends on

the temperature  $T$  in general, and hence, the  $T$  variation is also implicitly included in the system change.

### E. Fluctuation and dissipation relation

The LNS equation was introduced by Landau and Lifschitz in the context of the fluctuation-dissipation relation [28]. Here, we briefly discuss a relation between the LNS equation in Eq. (1) and the LNS equation in [28]. The Landau and Lifschitz LNS equation is not for a particle flowing in a fluid but for the fluid itself, so it has the same origin as Eq. (1). For such fluid fluctuations, Landau and Lifschitz assumed fluctuations in all fluid mechanical quantities such as the velocity, density, and pressure. The fluctuations in these quantities are introduced into the LNS equation via the divergence  $\sum_{k=1}^3 \partial s_{ik} / \partial x_k$  of a random stress  $s_{ij}$ , which is a component of the stress tensor  $\sigma'_{ij}$  and plays a role in a source of the fluctuations. In this sense, the  $\sum_{k=1}^3 \partial s_{ik} / \partial x_k$  term corresponds to the  $i$ -th component of  $\vec{\eta}(\vec{r}, t)$  in Eq. (1), where fluctuations are assumed only in the velocity and pressure because of the assumption of incompressibility. In addition, Landau and Lifschitz introduced a fluctuation dissipation relation using a random stress tensor  $s_{ij}$ . This point is also slightly different in our case; we assume the relation using  $\vec{\eta}(\vec{r}, t)$  such that

$$\langle \eta_i^\mu(t) \eta_j^\nu(t') \rangle = 2D \delta_{ij} \delta^{\mu\nu} \delta(t - t'), \quad (4)$$

where  $i$  and  $j$  denote space points and  $\mu$  and  $\nu$  represent directions. This relation is the same as that introduced in Ref. [25], except for the space dimension, and implies that the hydrodynamic fluctuation activation force varies slightly and changes instantly in the space and time directions compared to the characteristic scales in space and time in the reference physical system. The physical system in our case corresponds to a set of fluid particle lumps that move with  $\vec{V}$ , as described by Eq. (1), and the randomly changing forces come from the thermally fluctuating water molecules. Thus, the LNS equation in Eq. (1), which is limited to Newtonian fluids, is considered to be the same as that of Landau and Lifschitz because fluctuations are assumed in the velocity and pressure and activated by random forces.

Now, we briefly discuss the Einstein-Stokes-Sutherland formula corresponding to Eq. (4) to evaluate the strength  $D(\text{m}^2/\text{s}^3)$  of Brownian motion described by our LNS equation in

Eq. (1). The discussion here follows those in Ref. [25], and the formula is given by

$$2D\tau_e^2(=D_{\text{dif}}) = \frac{k_B T}{6\pi\mu b}, \quad (5)$$

where  $\tau_e$  is the relaxation time for a lump of fluid particles, which is assumed to be a sphere of radius  $b$ , and the symbols  $k_B$  and  $T$  are the Boltzmann constant and temperature, respectively. This  $\tau_e$  is estimated only numerically at present [25]. On the right-hand side, the viscosity  $\mu(=\rho\nu)$  connected to the kinematic viscosity  $\nu(\text{m}^2/\text{s})$  in Eq. (1) represents a macroscopic dissipation, while  $D(\text{m}^2/\text{s}^3)$  or  $D_{\text{dif}}(\text{m}^2/\text{s})$ , which is a diffusion constant, on the left-hand side corresponds to the fluctuations obtained by the expectation in Eq. (4) for random forces corresponding to microscopic motions of water molecules. The constant  $D_{\text{dif}}(\text{m}^2/\text{s})$  corresponds to diffusion of the fluid lump. The denominator on the right-hand side comes from Stokes's formula for the resistance force of a particle of radius  $b$  in a flow field. Strictly, a lump of fluid is not a particle, and its shape deforms as it moves. However, we consider that this deformation speed is comparable to the velocity of the fluid lump, which is negligibly small compared to the space-time random motion of water molecules.

The discrete expression  $\sqrt{2D\Delta t}\vec{g}$  of the random force in Eq. (3) comes from the stochastic nature of  $\vec{\eta}(\vec{r}, t)$  characterized by Eq. (4). A detailed explanation of this expression  $\sqrt{2D\Delta t}\vec{g}$  can be discussed from the viewpoint of an impulse force (Appendix D).

### III. NUMERICAL RESULTS

#### A. Velocity distribution for $D=0$

First, we introduce the results obtained at  $D = 0$  on lattice A. The distributions or histograms  $h(V_z)$  of  $|V_z|$  and  $h(V)$  of  $V$  are plotted in Fig. 6(a) and (b), where the calculation technique for  $h(V_z)$  and  $h(V)$  is described in Appendix C. The plotted data are calculated from a single convergent configuration of  $\vec{V}$  and at a small number of data points as described in subsection II C. Therefore, small fluctuations are observed in the data. The shape of  $h(V_z)$  vs.  $|V_z|$  is nearly the same as that of  $h(V)$  vs.  $V$ . No peak is observed in  $h(V_z)$  and  $h(V)$ , which are determined only by the boundary fluid flow. Figure 6(c) shows the dependence of  $V_z(r, \theta)$  on the distance  $r$  from the center of the cross-section and  $\theta$  (Fig. 5). The solid



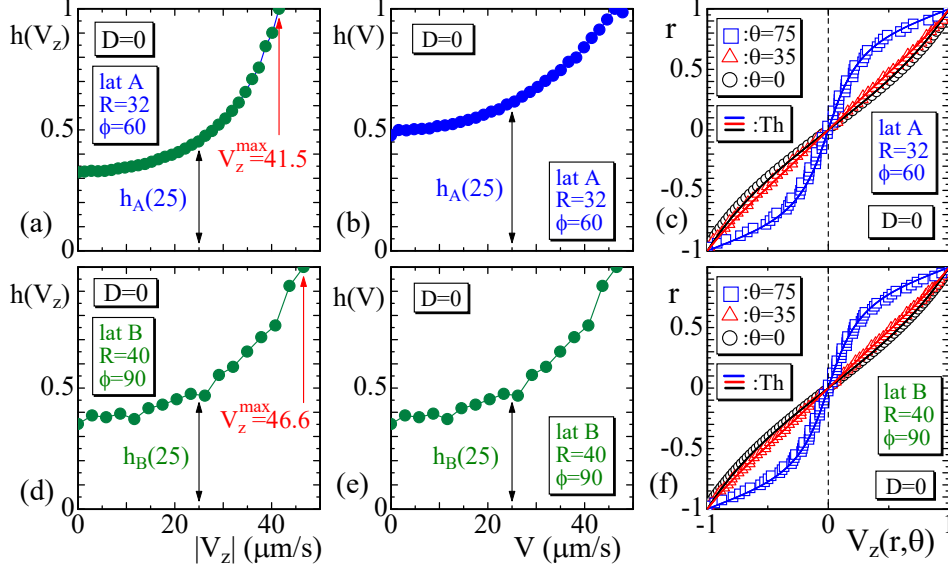


FIG. 6. Velocity distributions (a)  $h(V_z)$  vs.  $|V_z|$  and (b)  $h(V)$  vs.  $V$ , and (c) radial dependence of normalized  $V_z(r, \theta)$  obtained on lattice A; (d), (e), (f) those obtained on lattice B at  $D = 0$ . The results ( $\circ$ ) in (c) and (f) at  $\theta = 0$  correspond to the velocity distribution illustrated by the arrows in Fig. 2(a). The solid lines denoted as Th in (c) and (f) are drawn using Eq. (5).  $h(V_z)$  on lattice A in (a) is slightly smaller than that on lattice B in (d);  $h_A(25) < h_B(25)$ . This reflects the difference in the  $z$  component of the boundary velocity. In contrast,  $h(V)$  on lattice A in (b) is apparently larger than that on lattice B in (e);  $h_A(25) > h_B(25)$ , implying that the rotating boundary circulation enhances the flow velocity inside.

lines show theoretical predictions reported in Ref. [19] given by

$$V_z(r, \theta) = \frac{2}{\pi} V \tan^{-1} \left[ \frac{2(r/r_{\max}) \sin(90^\circ - \theta)}{1 - (r/r_{\max})^2} \right], \quad (0 \leq r \leq r_{\max}) \quad (5)$$

under the conditions  $r_{\max} = 1$  and  $V = 1$ , which are the normalized diameter and the normalized boundary velocity, respectively. The symbol  $\theta(^{\circ})$  is the angle shown in Fig. 5. We find that the simulation data are in good agreement with this theoretical prediction. Interestingly,  $V_z(r, \theta)$  is not influenced by the boundary velocity rotation. Moreover, as we see below, the Brownian motion of fluid particles ( $\Leftrightarrow$  nonzero  $D$ ) has no influence on  $V_z(r, \theta)$ .

The results obtained on lattice B are shown in Fig. 6(d)–(f). The distributions  $h(V_z)$  and  $h(V)$  in Fig. 6(d) and (e) are almost the same because the boundary velocity is along the  $z$  direction on lattice B. In contrast, they are slightly different from each other in Fig. 6(a) and (b) on lattice A, as expected from the boundary velocity rotating around the cylinder.

It is interesting to see that  $V_z^{\max}(=41.5)$  on lattice A is smaller than  $V_z^{\max}(=46.6)$  on lattice B, and moreover, that  $h(V_z)$  on lattice A is slightly smaller than that on lattice B for all  $V_z < 40(\mu\text{m/s})$  in Figs. 6(a), (d) as indicated by the up-down arrows at  $V_z = 25(\mu\text{m/s})$ . In contrast,  $h(V)$  on lattice A is apparently larger than that on lattice B for all  $V$  except for the velocities at  $h(V) = 1$  in Figs. 6(b), (e);  $h_A(25) > h_B(25)$ , as indicated by the up-down arrows. This difference is nontrivial and implies that the rotating fluid circulation enhances the flow velocity inside corresponding to the mixing enhancement [8–11]. The  $r$  dependencies of  $V_z(r, \theta)$  in Fig. 6(c) are the same as those in Fig. 6(f) and almost the same as those reported in Ref. [10]. We should note that the boundary velocities are not included in the calculations of  $h(V_z)$ ,  $h(V)$  and  $V_z(r, \theta)$ .

### B. Velocity distribution for $D \neq 0$

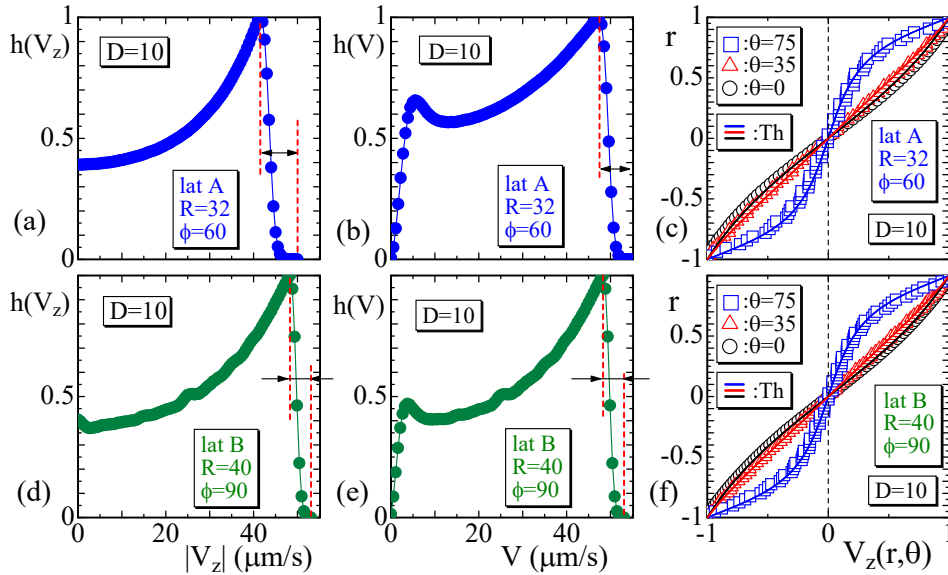


FIG. 7. (a)  $h(V_z)$  vs.  $|V_z|$ , (b)  $h(V)$  vs.  $V$ , and (c) radial dependence of normalized  $V_z(r, \theta)$  obtained on lattice A, and (d), (e), and (f) those obtained on lattice B.  $D$  is fixed to  $D=10$  in the simulation units. The solid lines denoted as Th in (c) and (f) are obtained from Eq. (5).

The results corresponding to  $D = 10$  are plotted in Fig. 7(a)–(c) for lattice A and Fig. 7(d)–(f) for lattice B. We find that  $h(V_z)$  and  $h(V)$  are apparently different from those plotted in Fig. 6 for both lattices A and B. Indeed,  $h(V_z)$  and  $h(V)$  drop to zero at

$V \simeq 45(\mu\text{m/s})$  in Fig. 7. This implies that there are fluid particles of velocities  $V_z > V_e \sin \phi^\circ$  and  $V > V_e = 50(\mu\text{m/s})$ , where  $\phi = 60^\circ(90^\circ)$  on lattice A (lattice B). The reason for the appearance of fluid particles of  $V_z > V_e \sin \phi^\circ$  and  $V > V_e$ , indicated by left-right arrows ( $\leftrightarrow$ ,  $\rightarrow\leftarrow$ ), is that the velocity of Brownian motion particles is a Gaussian distribution. Due to this nontrivial contribution, a tail of velocity appears in  $h(V_z)$  and  $h(V)$  in the regions of  $V_z > V_e \sin \phi$  and  $V > V_e$ . A drop of  $h(V)$  at  $V \simeq 10(\mu\text{m/s})$  is also a nontrivial influence of Brownian motion. The  $r$  dependence of  $V_z(r, \theta)$  is independent of lattices A and B, as shown in Fig. 7(c) and (f).

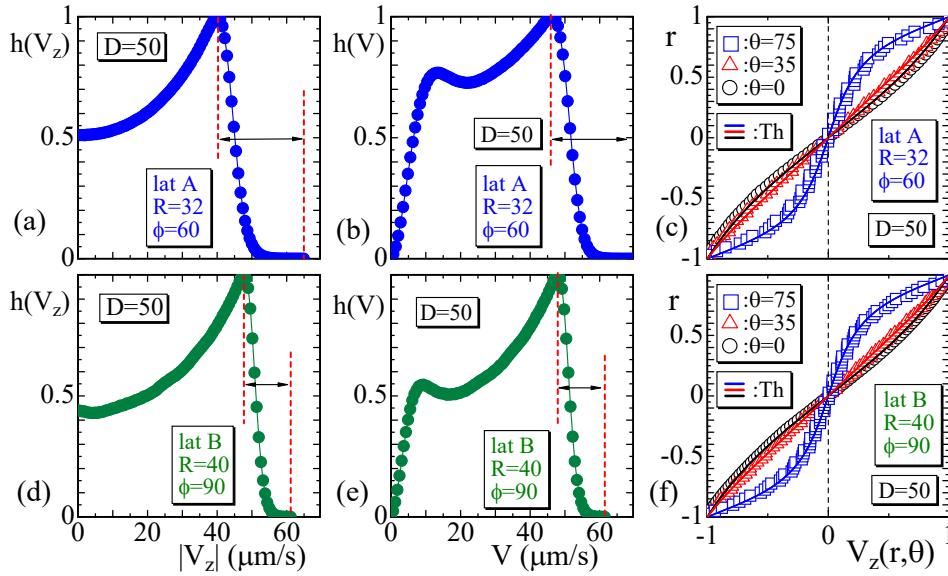


FIG. 8. (a)  $h(V_z)$  vs.  $|V_z|$ , (b)  $h(V)$  vs.  $V$ , and (c) radial dependence of normalized obtained on lattice A; (d), (e), and (f) those obtained on lattice B.  $D$  is fixed to  $D=50$  in the simulation units. The solid lines denoted as Th in (c) and (f) are obtained from Eq. (5).

Now, we plot the results corresponding to  $D=50$  obtained on lattices A and B in Fig. 8(a)–(c) and Fig. 8(d)–(f), respectively. Two peaks appear, as in the case of  $D=10$  in Figs. 7(b),(d), as an effect of the Brownian motion of fluid particles [24]. We find that the peak positions of  $V^{\text{peak}}$  of  $h(V)$  in Fig. 8(b) on lattice A are almost the same as those in Fig. 8(e) on lattice B. In contrast, the velocity regions larger than those peaks;  $V_z > V_z^{\text{peak}}$  and  $V > V^{\text{peak}}$  in Figs. 8(a),(b) indicated by ( $\leftrightarrow$ ), are wide compared to those in Figs. 8(d),(e) implying that the rotating fluid circulation is effective for the velocity enhancement. Moreover, the velocity regions of  $V_z > V_z^{\text{peak}}$  and  $V > V^{\text{peak}}$  are also wider

than those in the case of  $D=10$  in Fig. 7. This implies that a velocity enhancement due to Brownian motion becomes apparent with increasing  $D$ . The radial dependence of  $V_z(r, \theta)$  is still almost the same for lattices A and B even at  $D=50$ , as plotted in Fig. 8(c) and (f), and it is independent of  $D$ .

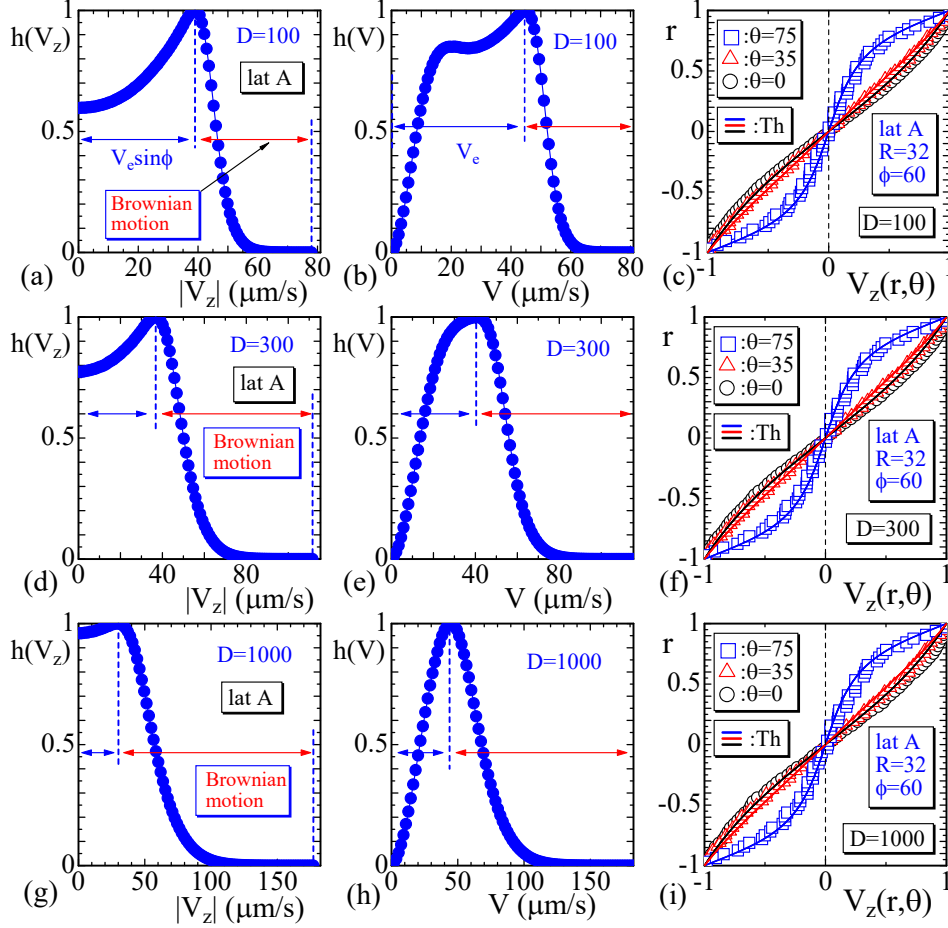


FIG. 9.  $h(V_z)$  vs.  $|V_z|$ ,  $h(V)$  vs.  $V$ , and radial dependence of normalized  $V_z(r, \theta)$  at (a)  $D=100$ , (b)  $D=300$ , (c)  $D=1000$  obtained on lattice A. The peak velocities  $V_z^{\text{peak}}$  and  $V^{\text{peak}}$  are slightly smaller than the the boundary velocities  $V_e \sin \phi = 50 \sin 60^\circ \simeq 43(\mu\text{m})$  and  $V_e = 50(\mu\text{m})$ . Enhancements of velocities, denoted by “Brownian motion” larger than the peak velocities, become apparent with increasing  $D$ .

To see the dependence on  $D$ , we further increase  $D$  to  $D=100$ ,  $D=300$  and  $D=1000$  and plot  $h(V_z)$  and  $h(V)$  in Figs. 9(a)–(h), where only results for lattice A are presented. In those larger  $D$  regions, effects of Brownian motion on the enhancement of flow velocity larger than the peak positions of  $h(V_z)$  and  $h(V)$  are apparent. In the figures, this enhancement

is denoted by the left-right arrows ( $\leftrightarrow$ ) with the symbol “Brownian motion”. The peak positions  $V_z^{\text{peak}}$  in  $h(V_z)$  and  $V^{\text{peak}}$  in  $h(V)$  are slightly smaller than the boundary velocities  $V_e \sin \phi = 50 \sin 60^\circ \simeq 43(\mu\text{m})$  and  $V_e = 50(\mu\text{m})$ . We should emphasize that the radial dependence of  $V_z(r, \theta)$  remains unchanged even for sufficiently large  $D$  such as  $D=1000$  as plotted in Figs. 9(c),(f) and (i). However, this is reasonable because the fluid particles at position  $(r, \theta)$  thermally fluctuate into isotropic directions with rapid velocity, and the mean value  $V_z(r, \theta)$  is determined only by the boundary flow.

### C. Streaming velocities under $D$ variation and mixing enhancement

First, we show the maximum velocities  $V_z^{\text{max}}$  and  $V^{\text{max}}$  obtained on lattices A and B in Fig. 10(a) and (b), where  $V_z^{\text{max}}$  denotes the absolute maximum of the  $z$  component of  $\vec{V}$ . We find from Fig. 10(a) that  $V_z^{\text{max}}(\text{lat B}) > V_z^{\text{max}}(\text{lat A})$  for a sufficiently small  $D$  region. This relation comes from the fact that the boundary velocity rotates on lattice A, while it is along the  $z$  direction on lattice B. We also find from Fig. 10(b) that the  $V^{\text{max}}$  on lattice A becomes larger than that on lattice B for  $D \geq 10$ , although these values are almost the same for sufficiently small  $D$ . This result  $V^{\text{max}}(\text{lat A}) > V^{\text{max}}(\text{lat B})$  implies that the fluid circulation effectively decreases  $D$ . This effective decrement of  $D$  means that the maximum flow velocity under the rotating circulation at  $D_1$  is the same as that under the parallel circulation at a higher  $D_2(> D_1)$ . Recalling  $D \propto 1/\mu$  in Eq. (5), and by letting  $\mu_1, \mu_2$  be  $D_1 \propto 1/\mu_1$  and  $D_2 \propto 1/\mu_2$ , we have  $\mu_1 > \mu_2$ . Therefore, the results in Figs. 10(a),(b) indicates that the maximum flow velocity of fluid with high viscosity  $\mu_1$  under the rotating circulation is the same as that of relatively low viscosity  $\mu_2$  under the non-rotating circulation.

To see the velocities  $|V_z|(< V_z^{\text{max}})$  and  $V(< V^{\text{max}})$ , we plot  $h(V_z)$  and  $h(V)$  in Figs. 10(c),(d) and Figs. 10(e),(f), respectively. The areas  $\int_0^{V_z^{\text{max}}} h(V_z) dV_z$  and  $\int_0^{V^{\text{max}}} h(V) dV$  are calculated using the numerical integration of Simpson’s rule and plotted in Figs. 10(g),(h). The areas correspond to the absolute transport of fluids per second along the  $z$  direction and that along the  $\vec{V}$  direction. The dashed horizontal lines drawn in Fig. 10(h) at  $D=0$  without Brownian motion indicate that the rotational circulation enhances the mixing [8–11]. We should note that the areas for  $D > 0$  are larger than the dashed lines and increase with increasing  $D$ . This monotonically increasing property in the areas implies an enhancement

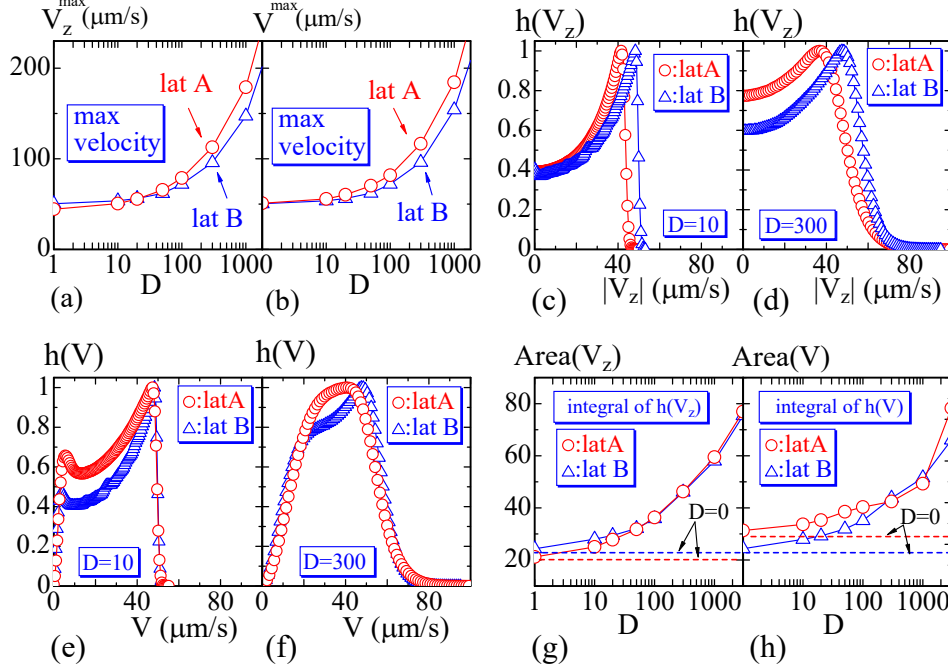


FIG. 10. Maximum velocities (a)  $V_z^{\max}$  vs.  $D$  and (b)  $V^{\max}$  vs.  $D$  obtained on lattices A and B. The magnitude relation  $V_z^{\max}(B) > V_z^{\max}(A)$  is reversed to  $V_z^{\max}(B) < V_z^{\max}(A)$  at  $D \simeq 20$  in (a), and the difference in  $V^{\max}$  begins to appear at  $D \simeq 10$  in (b). The distribution of  $h(V_z)$  vs.  $|V_z|$  on lattices A and B obtained at (c)  $D = 10$ , (d)  $D = 300$ , and  $h(V)$  vs.  $V$  at (e)  $D = 10$  and (f)  $D = 300$ . (g)  $\text{Area}(V_z) = \int_0^{V_z^{\max}} h(V_z) dV_z$  and (h)  $\text{Area}(V) = \int_0^{V^{\max}} h(V) dV$  obtained through numerical integrations. The dashed horizontal lines indicate the areas at  $D = 0$ .

of mixing by Brownian motion. Moreover, we find that

$$\int_0^{V_z^{\max}(\text{lat A})} h_A(V_z) dV_z \simeq \int_0^{V_z^{\max}(\text{lat B})} h_B(V_z) dV_z, \quad (D > 50), \quad (6)$$

$$\int_0^{V^{\max}(\text{lat A})} h_A(V) dV > \int_0^{V^{\max}(\text{lat B})} h_B(V) dV, \quad (D < 300). \quad (7)$$

The first relation means that the absolute transport along the  $z$  direction of lattice A is almost comparable with that of lattice B for  $D > 50$ . Comparing the result in Eq. (6) for  $D > 50$  and the plotted data of  $\int_0^{V_z^{\max}(\text{lat A})} h_A(V_z) dV_z < \int_0^{V_z^{\max}(\text{lat B})} h_B(V_z) dV_z$  in Fig. 10(g) for  $D < 50$ , we find that the rotating boundary circulation helps mixing of biological materials even in high viscosity medium under Brownian motions of fluid particles. In addition to this enhancement, the inequality in Eq. (7) means that the absolute transport along the  $\vec{V}$  direction of lattice A is larger than that of lattice B for  $D < 300$ . It is also interesting to see that the region  $50 < D < 300$  of mixing enhancements in Eqs. (6) and (7) is included in the

experimentally relevant region  $D$ , which will be shown in the following subsection.

#### D. Velocity distribution considering $D$ variation

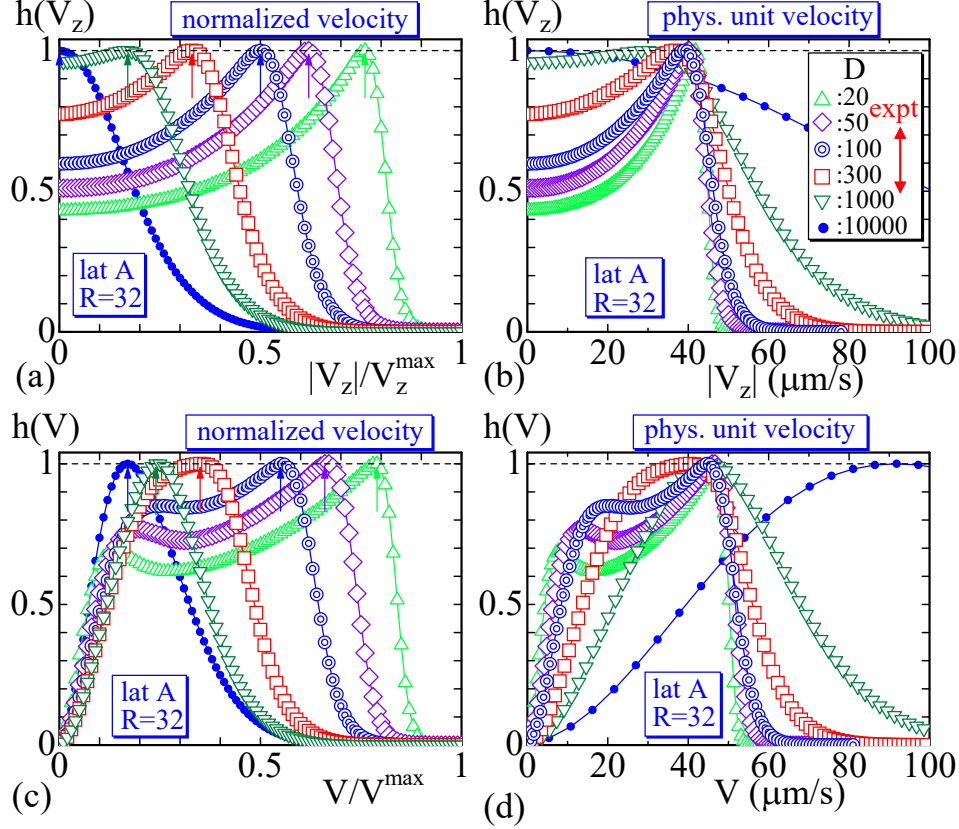


FIG. 11. (a)  $h(V_z)$  vs. the normalized  $|V_z|/V_z^{\max}$  and (b)  $h(V_z)$  vs.  $|V_z|$  obtained for  $20 \leq D \leq 10^4$  on lattice A. (c)  $h(V)$  vs. the normalized  $V/V^{\max}$  and (d)  $h(V)$  vs.  $V$ . The peak positions  $|V_z|/V_z^{\max}$  and  $V/V^{\max}$  are indicated by vertical arrows in (a) and (c). The peaks are approximately  $V_z^{\text{peak}} = 40(\mu\text{m/s})$  in (b) and  $V^{\text{peak}} = 46(\mu\text{m/s})$  in (d). These values are slightly smaller than the boundary velocities  $43(=V_e \sin 60^\circ)(\mu\text{m/s})$  and  $50(\mu\text{m/s})$ , respectively. The up-down arrow with “expt” in (b) denotes the experimentally relevant region in the sense that the shape of  $h(V_z)$  is relatively close to the experimentally observed shapes in Figs. 2(c), (d).

In this subsection, we analyze the dependence of the peak velocities on  $D$  and discuss whether the peak positions are influenced by thermal fluctuations of fluid particles to find  $D$  which is suitable to the system under consideration in the sense that the shape of  $h(V_z)$  is close to the experimental ones in Figs. 2(c), (d).

Figures 11(a),(b) show  $h(V_z)$  vs. the normalized  $|V_z|/V_z^{\max}$  and  $|V_z|$  obtained at several points of  $D$  in the range  $20 \leq D \leq 10^4$  on lattice A. The distributions  $h(V)$  are also plotted in Figs. 11(c), (d) with  $V/V^{\max}$  and  $V$ . The upward arrows in Figs. 11(a), (c) indicate the peak positions  $V_z^{\text{peak}}$  and  $V^{\text{peak}}$ . We find that the peak positions in Figs. 11(b), (d) remain almost unchanged under the variation of  $D$ , and these are close to or slightly smaller than  $V_e \cos 60^\circ \simeq 43(\mu\text{m/s})$  and  $V_e = 50(\mu\text{m/s})$ , respectively, in the range of  $D \leq 1000$  at least. The up-down arrow in Fig. 11(b) indicates the experimentally relevant region of  $D$ , where the shape of  $h(V_z)$  is relatively close to the experimental ones in Figs. 2(c), (d).

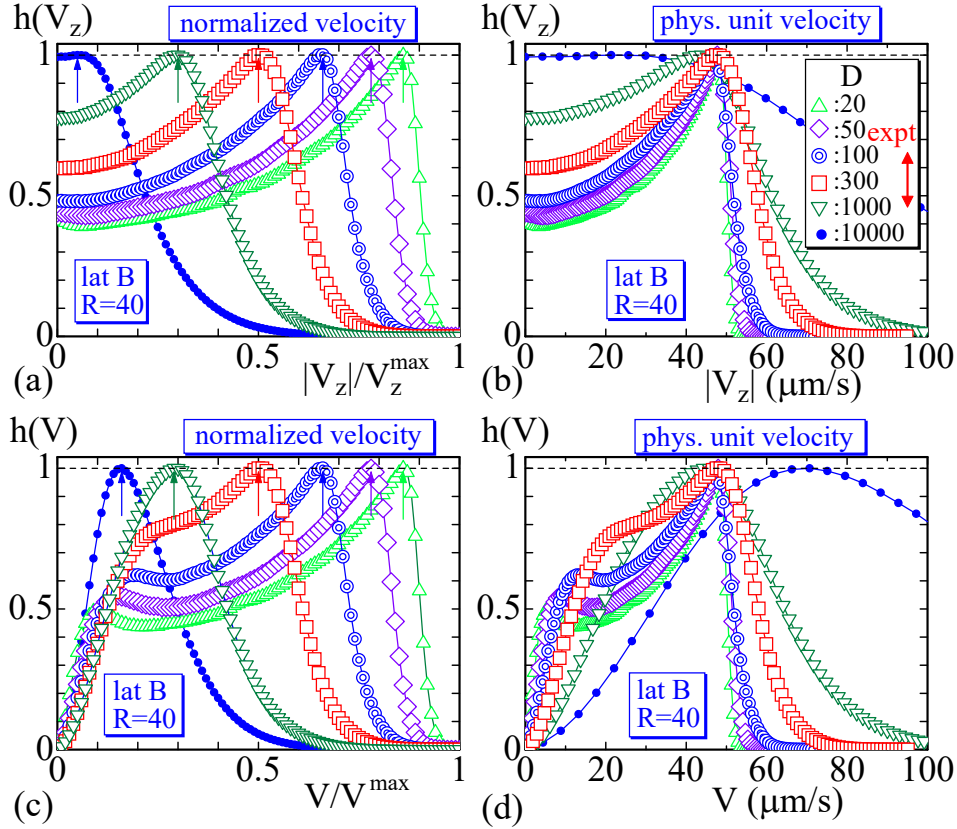


FIG. 12. (a)  $h(V_z)$  vs. the normalized  $|V_z|/V_z^{\max}$  and (b)  $h(V_z)$  vs.  $|V_z|$  obtained for  $10 \leq D \leq 10^4$  on lattice B. The peak positions  $V_z$  and  $V$  are indicated by vertical arrows. (c)  $h(V)$  vs. the normalized  $V/V^{\max}$  and (d)  $h(V)$  vs.  $V$ . The peaks are approximately  $V_z^{\text{peak}} = V^{\text{peak}} = 47(\mu\text{m/s})$  in both  $h(V_z)$  and  $h(V)$ . The peak value is slightly smaller than the boundary velocity  $50(\mu\text{m/s})$  on lattice B. The up-down arrows with “expt” denote the experimentally relevant region, and the corresponding value of  $D$  is slightly larger than that on lattice A shown in Fig. 11(b).

We plot the  $h(V_z)$  and  $h(V)$  results obtained on lattice B in Figs. 12(a)–(d). The



horizontal axes are the normalized and the physical unit of  $|V_z|$  and  $V$ . The peak positions  $V_z^{\text{peak}}$  of  $h(V_z)$  and  $V^{\text{peak}}$  of  $h(V)$ , indicated by arrows in Figs. 12(a), (c), are the same owing to the fact that the boundary velocity is parallel to the  $z$  axis on lattice B. These peaks are approximately equal to  $V_z^{\text{peak}} = V^{\text{peak}} = 47(\mu\text{m/s})$  for  $D \leq 300$  in Figs. 12(b), (d). This value is slightly smaller than the boundary velocity  $50(\mu\text{m/s})$ . We find that the shape of  $h(V_z)$  at  $D = 300$  is relatively close to the experimentally observed one, and hence, the experimentally relevant region of  $D$ , indicated by the up-down arrow in Fig. 12(b), moves to slightly larger region compared to that on lattice A shown in Fig. 11(b). This shift of the “expt” region is also expected from the results in Figs. 10(a), (b)

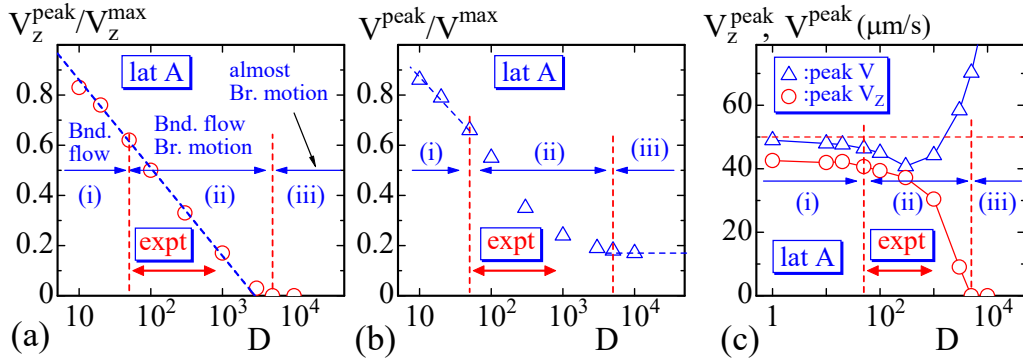


FIG. 13. (a), (b) Variations in the normalized peaks  $V_z^{\text{peak}}/V_z^{\text{max}}$  and  $V^{\text{peak}}/V^{\text{max}}$  vs. log-scale of  $D$ , and (c)  $V_z^{\text{peak}}$  and  $V^{\text{peak}}$  vs. log scale of  $D$ , where the horizontal dashed line represents the boundary velocity  $V_e = 50(\mu\text{m/s})$ , which is non-parallel to the  $z$  axis. The left-right arrows with “expt” indicate a region of  $D$ , where the shape of  $h(V_z)$  is relatively close to the experimentally observed ones. The vertical dashed lines roughly separate the  $D$  region into three different regions, where the streaming is mainly activated by (i) boundary flow, (ii) boundary flow and Brownian motion, and (iii) Brownian motion.

The peak positions  $V_z^{\text{peak}}/V_z^{\text{max}}$  in  $h(V_z)$  are plotted in log scale in Fig. 13(a). Only results of lattice A are presented for simplicity. We find that that the range of  $D$  can be divided into three different regions (i), (ii) and (iii). In the region (i), the fluid particles are mainly influenced by the boundary flows because  $D$  is relatively small, and the peak values  $V_z^{\text{peak}}$  are expected to be close to the boundary velocity  $V_e \sin 60^\circ = 43(\mu\text{m/s})$ . The region (ii) is the range of  $D$  for  $V_z^{\text{peak}}/V_z^{\text{max}} < 0.7$ , where the fluid particles are influenced by both the boundary flow and Brownian motion, and denoted by “Bnd. flow, Br. motion” in the

figure. The region (iii) is the range of  $D \geq 5 \times 10^3$  for  $V_z^{\text{peak}} \simeq 0$ , where the fluid particles are influenced mostly by Brownian motion, and is denoted by “almost Br. motion”. The left-right arrow ( $\leftrightarrow$ ) with “expt” denotes the experimentally relevant region  $50 \leq D < 1000$ , where the shape of  $h(V_z)$  is relatively close to the experimentally reported ones. We observe a scaling of  $V_z^{\text{peak}}/V_z^{\text{max}}$  such as  $V_z^{\text{peak}}/V_z^{\text{max}} \sim -\alpha \log D$  ( $\alpha \simeq 1.52$ ) in the region  $20 \leq D \leq 1000$ . Interestingly, this region includes the experimentally relevant region of  $D$ .

Figure 13(b) plots the  $V^{\text{peak}}/V^{\text{max}}$  peaks in  $h(V)$  of  $D$  on a log scale. The positions of the vertical dashed lines separating regions (i), (ii) and (iii) and of the horizontal left-right arrow are the same as those in Fig. 13(a). We find that the peak position goes down to  $V^{\text{peak}}/V^{\text{max}} \rightarrow 0.17$  in region (iii), as expected from the plots in Fig. 11(c). No scaling relation is observed in  $V^{\text{peak}}/V^{\text{max}}$  in region (ii). Figure 13(c) plots the peaks  $V^{\text{peak}}$  and  $V_z^{\text{peak}}$  with the physical unit ( $\mu\text{m/s}$ ), where the dashed vertical lines and the left-right arrow are the same as in Figs. 13(a), (b) and the dashed horizontal line denotes the boundary velocity  $V_e = 50(\mu\text{m/s})$ . These values  $V^{\text{peak}}$  and  $V_z^{\text{peak}}$  are also listed in Table IV with  $D$  and the corresponding  $D_e$  in the physical unit.

TABLE IV. Assumed parameters  $D$  and  $D_{e,0}$  in the simulation unit and physical unit, the peak values  $V_z^{\text{peak}}$  and  $V^{\text{peak}}$  of  $h(V_z)$  and  $h(V)$  on lattice A in Fig. 13(c) and Figs. 11(b), (d).

| $D$  | $D_{e,0}$               | $V_z^{\text{peak}}(\text{lat A})$ | $V^{\text{peak}}(\text{lat A})$ |
|--|-------------------------|-----------------------------------|---------------------------------|
| $\frac{(\alpha_0 \text{m})^2}{(\beta_0 \text{s})^3}$ | $\text{m}^2/\text{s}^3$ | $\mu\text{m/s}$                   | $\mu\text{m/s}$                 |
| 20   | $1.25 \times 10^{-6}$   | 42.2                              | 47.6                            |
| 50   | $3.13 \times 10^{-6}$   | 40.7                              | 46.4                            |
| 100  | $6.25 \times 10^{-6}$   | 39.4                              | 45.0                            |
| 300  | $1.88 \times 10^{-5}$   | 37.2                              | 40.8                            |
| 1000   | $6.25 \times 10^{-5}$   | 30.4                              | 44.3                            |
| 3000   | $1.88 \times 10^{-4}$   | 9.05                              | 58.4                            |
| 5000   | $3.13 \times 10^{-4}$   | 0.0                               | 70.2                            |

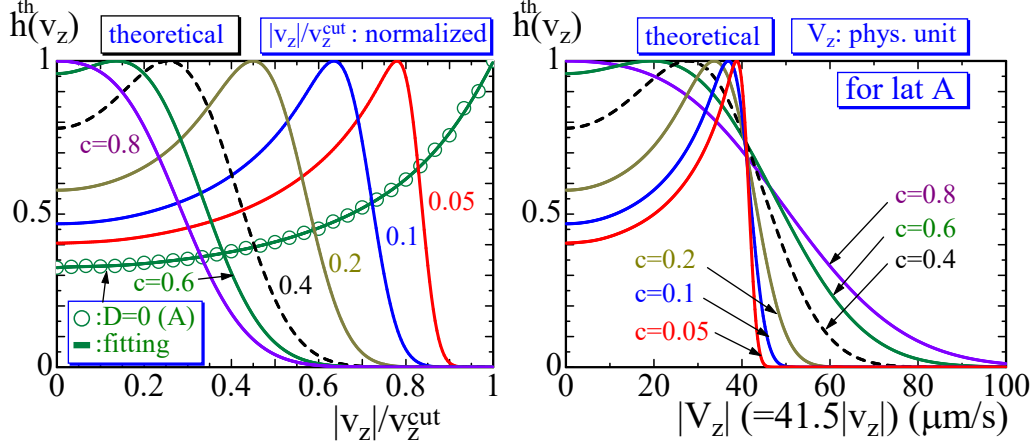


FIG. 14. (a) Velocity distributions  $h^{\text{th}}(v_z)$  vs. the normalized  $|v_z|/v_z^{\text{cut}}$  calculated using Eq. (8) with several values of  $c$  corresponding to the Maxwell-Boltzmann distribution  $f(v_z) \propto \exp(-v_z^2/c^2)$ . Plotted circles ( $\bigcirc$ ) are obtained by normalizing the simulation results of  $h(V_z)$  at  $D=0$  in Fig. 6(a) and the corresponding solid line indicated by an arrow is drawn by fitting with a polynomial function  $h_0(v_z)$  (Appendix E). (b)  $h^{\text{th}}(v_z)$  vs.  $|V_z| (=41.5|v_z|)$  ( $\mu\text{m/s}$ ). We find that the curves with  $c=0.2$  and  $c=0.4$  are relatively close to the experimentally observed one.

### E. Theoretical prediction of the velocity distribution

To check that the simulation results are reasonable and estimate the size of fluid particles, we calculate a theoretical distribution  $h^{\text{th}}(v_z)$  of  $v_z$  by

$$h^{\text{th}}(v_z) \propto \int_{-1}^1 h_0(u) \exp[-(v_z - u)^2/c^2] du, \quad (8)$$

$$h_0(u) = \text{polynomial function},$$

$$(u = 1 \Leftrightarrow V_z = 41.5(\mu\text{m/s})),$$

where  $h_0$  is a polynomial function of  $u (=V_z/41.5)$ , which is a normalized velocity (Appendix E), fitting the simulation result  $h(u)$  on lattice A at  $D=0$  corresponding to  $h(V_z)$  in Fig. 6(a), where the maximum velocity  $V_z^{\text{max}} = 41.5(\mu\text{m/s})$  is indicated by an arrow. This  $h_0(u)$  represents the effect of the boundary flow. The meaning of  $\exp[-(v_z - u)^2/c^2]$ , denoted by  $f(v_z, u)$ , is the Maxwell-Boltzmann distribution of fluctuating velocity  $v_z$  of particles moving with the mean velocity  $u (= \langle v_z \rangle)$ . In the expression of  $h^{\text{th}}(v_z)$ , the unit velocity is assumed as  $v_z = 1 \Leftrightarrow V_z = 41.5(\mu\text{m/s})$ . The constant  $c$  in the exponential function is the peak position of the Maxwell-Boltzmann distribution  $f(v) \propto v^2 \exp(-v^2/c^2)$  (Appendix E). The reason

of the multiplication of  $h_0(u)$  and that of the replacement  $v_z^2$  in  $f(v_z, u=0)$  to  $(v_z - u)^2$  in  $f(v_z, u)$  are to include effects of Brownian motion of all moving particles with mean velocity  $|u| \leq 1$  into the distribution  $h^{\text{th}}(v_z)$ , in which  $v_z$  is not always limited to  $|v_z| \leq 1$ . To be more specific, the expression  $h_0(u)du$  for  $|u| \leq 1$  is the total number of particles with mean velocity between  $u$  and  $u + du$ , and  $\exp[-(v_z - u)^2/c^2]$  is the contribution of the moving particles of velocity  $u$  to  $h^{\text{th}}(v_z)$ , and these contributions can be integrated out in the range  $-1 \leq u \leq 1$ . In this calculation, we simply assume that the particles move with velocities of the distribution  $h_0(u)$  along the  $z$  axis, and hence, no interaction of the particles with fluids is assumed.

Figure 14(a) shows the calculated  $h^{\text{th}}(v_z)$  vs. the normalized  $|v_z|/v_z^{\text{cut}}$ , where not only the height but also the horizontal axes are normalized with the cutoff velocity  $v_z^{\text{cut}}$ . The height normalization is numerically easy because there are peaks in  $h^{\text{th}}(v_z)$ , while the tail of the exp function extends to  $v_z \rightarrow \infty$  in contrast to the simulation data  $h(V_z)$  in Fig. 11(a). Here, the cutoff of  $h^{\text{th}}(v_z)$  is assumed to  $h^{\text{th}}(v_z^{\text{cut}}) = 1 \times 10^{-8}$  to find the cutoff velocity  $v_z^{\text{cut}}$  for the normalization of the  $|v_z|$  axis. The  $h^{\text{th}}(v_z)$  is also plotted with the physical unit of  $|V_z| (= 41.5|v_z|)$  in Fig. 14(b), where the same symbol  $V_z$  is used here in the physical unit as that of the simulation data  $h(V_z)$ .

TABLE V. Assumed value  $c$  of the Maxwell Boltzmann distribution  $f(v_z) \propto \exp(-v_z^2/c^2)$ , and the velocity  $u^{\text{MB}}$  ( $\mu\text{m/s}$ ) corresponding to the peak of  $f(v) \propto v^2 \exp(-v^2/c^2)$ , the peak velocity  $V_z^{\text{peak}}$  of  $h^{\text{th}}(v_z)$ , the mass  $m$ , and the size  $d_{\text{fluid}}$  ( $\mu\text{m}$ ) of fluid particles. All  $d_{\text{fluid}}$  ( $\mu\text{m}$ )'s are smaller than the upper limit  $100(\mu\text{m})$  for thermally fluctuating particles. The peak velocities  $V_z^{\text{peak}}$  are slightly smaller than but comparable with the simulation results in Figs. 11(b), 13(c) and in Table IV.

| $c$ | $u^{\text{MB}}$ ( $\mu\text{m/s}$ ) | $V_z^{\text{peak}}$ ( $\mu\text{m/s}$ ) | $m$ (kg)               | $d_{\text{fluid}}$ ( $\mu\text{m}$ ) |
|-----|-------------------------------------|---|------------------------|--------------------------------------|
| 0.1 | 4.30                                | 36.9                                    | $4.48 \times 10^{-13}$ | 76                                   |
| 0.2 | 8.60                                | 33.7                                    | $1.12 \times 10^{-13}$ | 48                                   |
| 0.4 | 17.2                                | 27.7                                    | $2.80 \times 10^{-14}$ | 30                                   |
| 0.6 | 25.8                                | 19.5                                    | $1.24 \times 10^{-14}$ | 23                                   |
| 0.8 | 34.4                                | 0.0                                     | $7.00 \times 10^{-14}$ | 19                                   |

We find that the curves in Figs. 14(a), (b) are relatively similar to those simulation

results in Figs. 11(a), (b). This similarity implies that the shape of simulation data in Figs. 11(a), (b) reflects the effects of Brownian motion of fluid particles. In other words, the assumed fluid particles undergo thermal fluctuations according to the Maxwell Boltzmann distribution. To be specific, the curve with  $c = 0.2$  in Fig. 14(b) is almost close to the simulation result  $h(V_z)$  at  $D = 100$  in Fig. 11(b), which is close to the experimental ones in Figs. 2(c), (d). This resemblance implies that the peak position  $u^{\text{MB}}$  of  $f(V)$  for  $D = 100$  is  $u^{\text{MB}} = c = 0.2$  with the unit of  $41.5(\mu\text{m/s})$ . The corresponding fluid particle size  $d_{\text{fluid}}$  is approximated to  $d_{\text{fluid}} \simeq 48(\mu\text{m})$  (Appendix E), which is meaningful only in the LNS simulations for the streaming under consideration. We calculate  $d_{\text{fluid}}$  for several different values of  $c$  and list them in Table V. The peak positions  $V_z^{\text{peak}}(\mu\text{m/s})(=41.5v_z^{\text{peak}})$  of  $h^{\text{th}}(v_z)$  in the region  $0.2 \leq c \leq 0.4$  are almost comparable with or slightly smaller than  $V_z^{\text{peak}}$  of  $h(V_z)$  in the region  $50 \leq D \leq 1000$  in Table IV. This consistency strongly suggests that there exists a unique  $D$  close to  $D = 100$  representing thermal fluctuations in the protoplasmic streaming under study. We should note that  $h^{\text{th}}(v_z)$ 's obtained by replacing  $h_0(u)$  corresponding to  $h(V_z)$  on lattice B in Fig. 6(d) remain almost unchanged from those plotted in Figs. 14(a), (b).

## F. Snapshots of the velocity and pressure

We show snapshots of the velocity and pressure obtained on the cross-section of the cylinder at  $z = L/2$  on lattice A for several different  $D$  values. The direction of the boundary velocity at  $z = L/2$  is the opposite to that on the boundaries  $\Gamma_1$  at  $z = 0$  and  $\Gamma_2$  at  $z = L$  (Fig. 3(a)). The velocities denoted by the cones in Figs. 15(a)–(d) are of convergent configurations corresponding to (a)  $D = 0$ , (b)  $D = 20$ , (c)  $D = 100$  and (d)  $D = 1000$ . For clear visualization, only the velocities at every other vertex are shown. The pressures  $p$  are normalized to  $0 \leq p \leq 1$  and represented by the color gradation. In this normalization, the boundary pressure  $p = 0$  changes to  $p \simeq 0.5$ . Because the  $z$  component of the velocity is negative  $V_z < 0$  in the lower part of the cross-section, the velocities are hidden behind the cross-sectional surfaces for the pressure visualization.

An examination of Fig. 15(a) shows that the fluid regularly flows according to the boundary velocity, and the pressure  $p$  remains almost unchanged from the boundary pressure  $p(\simeq 0.5)$  at  $D = 0$ . The velocity and pressure are confirmed to be disturbed at nonzero  $D$ ,

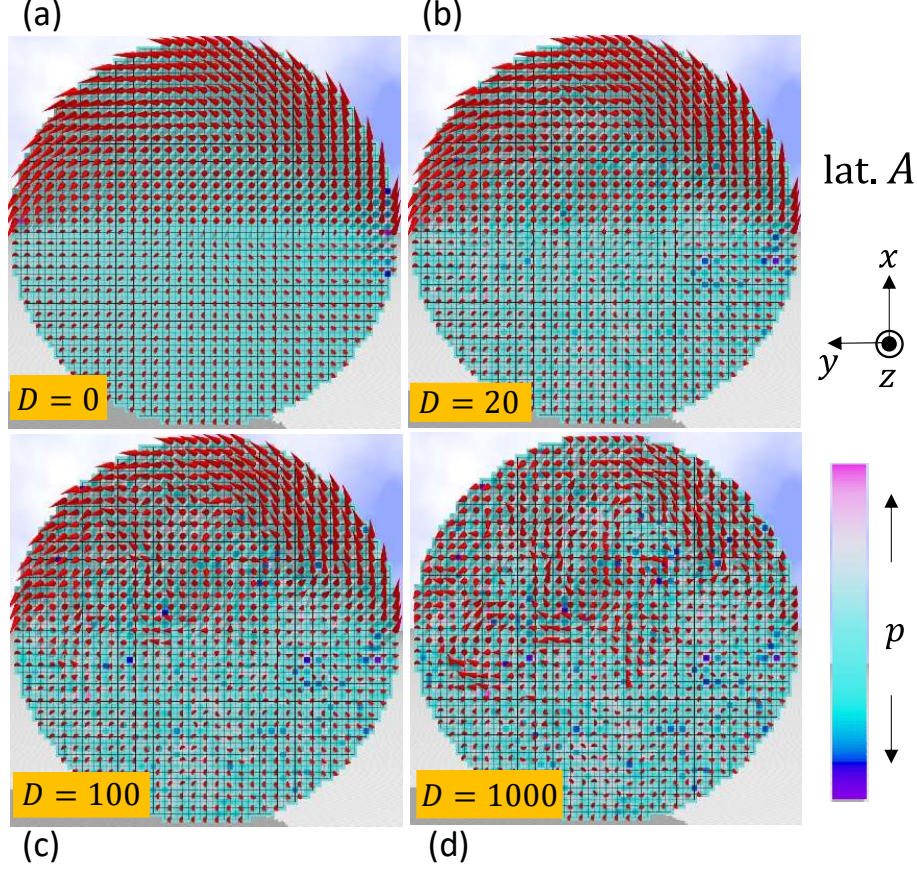


FIG. 15. Snapshots of the velocity and pressure obtained on lattice A at the cross-section at the middle of the cylinder  $z = L/2 (\simeq 179)$ . Velocities with pressure corresponding to (a)  $D = 0$ , (b)  $D = 20$ , (c)  $D = 100$ , and (d)  $D = 1000$ . The small red cones represent the velocity. Only the velocities at every other vertex are shown.

and the disturbance becomes stronger when  $D$  increases.

The pressure at higher  $D$  does not always vary smoothly but is randomly distributed over the cross-section. This condition of the pressure configuration is relatively close to that of Couette flow between parallel plates, which was obtained using 2D LNS simulations [26].

To visualize the difference in velocity configuration  $\vec{V}$  between lattices A and B, we show snapshots of velocity  $\vec{V}$  and pressure  $p$  obtained on lattice B in Figs. 16(a)–(d). The velocities in Figs. 16(a)–(d) are shown at every third vertex. Because  $p \simeq 0.5$  at every point on the cross-section at  $D=0$  in the convergent configuration, we show snapshots of  $\vec{V}$  and  $p$  at  $D=1$  instead of those at  $D=0$  in Fig. 16(a). The velocity configurations on lattice B are clearly different from those on lattice A for all  $D$ , as expected from the difference in the



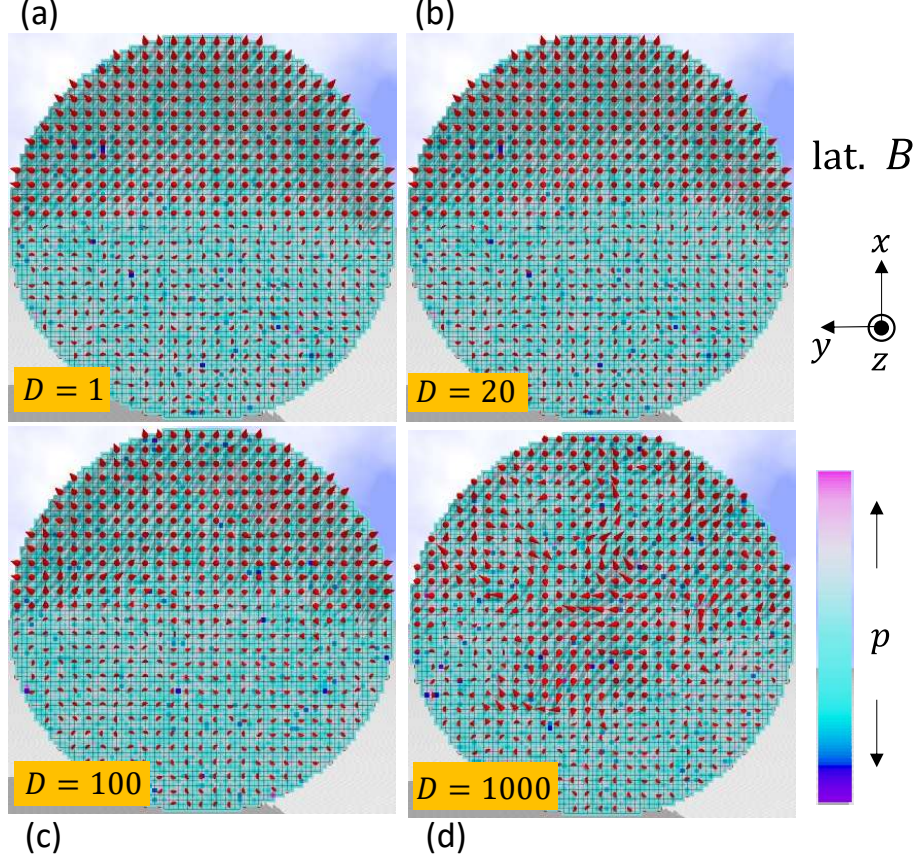


FIG. 16. Snapshots of velocity and pressure obtained on lattice B at the cross-section of the middle of the cylinder  $z = L/2 (= 40)$ . Velocity and pressure corresponding to (a)  $D = 1$ , (b)  $D = 20$ , (c)  $D = 100$ , and (d)  $D = 1000$ . The small red cones represent the velocity. Only the velocities at every third vertex are shown.

boundary condition for  $\vec{V}$ .

#### IV. SUMMARY AND CONCLUSION

In this paper, we numerically study the velocity distribution for protoplasmic streaming in plant cells using LNS simulations on 3D cylinders discretized by regular cubic lattices. The goal of our study was to determine whether experimentally observed and reported peaks in the velocity distribution can be reproduced using LNS simulations. Additionally, we were interested in whether the circular motion of fluid over the surfaces of cells has nontrivial effects on the flows inside the cells.

The velocity distributions  $h(V_z)$  of  $|V_z|$  along the longitudinal direction of the cylinder and  $h(V)$  of the velocity magnitude  $V(=|\vec{V}|)$  are calculated on two different lattices A and B. We calculate  $h(V_z)$  for  $|V_z|$  simply by assuming  $h(V_z)=h(-V_z)$  because of the expected symmetry  $V_z \rightarrow -V_z$  in  $h(V_z)$ . The distributions  $h(V_z)$  and  $h(V)$  are calculated on all cross sections of lattice. The radial dependence of  $\vec{V}_z$  is also calculated at angles  $\theta$  from the vertical direction of  $\theta=0^\circ, 35^\circ, 75^\circ$  on the cross section at the center of longitudinal lattice direction. The boundary velocity rotates on the cylindrical surface on lattice A, while it is parallel to the longitudinal direction on lattice B. The strength  $D$  of random Brownian motion is varied in the range of  $0 \leq D \leq 10000$  as an input parameter.

We find a peak in  $h(V_z)$  for  $D \geq 10$ , and this peak corresponds to the boundary velocity at least in the region  $10 \leq D \leq 1000$ . The shape of  $h(V_z)$  on lattice A in the range  $50 \leq D \leq 1000$  is relatively close to the reported experimental data. We also find two different peaks in  $h(V)$  at two different velocities  $V_1$  and  $V_2$  ( $V_1 < V_2$ ) when  $D$  is increased to  $10 \leq D \leq 100$  or greater, where  $V_2$  corresponds to the boundary velocity. The Brownian motion of fluid particles is reflected in the emergence of the first peak in  $h(V)$  at  $V_1$  and the second peak of  $h(V)$  at  $V_2$  such that the curve  $h(V)$  has a tail for  $V > V_2$ . This appearance of fluid particles at velocities  $V > V_2$  higher than the boundary velocity  $V_2$  is also a nontrivial effect of Brownian motion and is expected to play a nontrivial role in enhancing mixing.

On the enhancement of mixing, we calculate the absolute transports of fluids along the longitudinal direction and the direction of  $\vec{V}$  on both lattices A and B by varying  $D$ . We confirm from these calculations that the mixing of biological materials is enhanced by Brownian motion of fluid particles and also by the rotating circular motion of boundary fluids with the help of Brownian motion. Importantly, the mixing is improved under the presence of Brownian motion of the fluid particles.

To check that the simulation data  $h(V_z)$  are reasonable, we theoretically calculate  $h^{\text{th}}(v_z)$  with a normalized  $v_z$  using the simulation data  $h(V_z)$  for  $D=0$  and the Maxwell Boltzmann distribution of  $v_z$  for moving particles. The results  $h^{\text{th}}(v_z)$  are consistent with simulation data  $h(V_z)$ . From this analysis, we confirm that the LNS simulation in this paper suitably implement the thermal fluctuations of fluid particles for protoplasmic streaming, and we also find that the size of fluid particles is in the range of  $20(\mu\text{m}) \sim 50(\mu\text{m})$ .



## ACKNOWLEDGMENTS

H.K. acknowledges Fumitake Kato for discussions. This work was supported in part by Collaborative Research Project J20Ly09 at the Institute of Fluid Science (IFS), Tohoku University, and in part by a Collaborative Research Project at the National Institute of Technology (KOSEN), Sendai College. Numerical simulations were performed on the "AFINITY" supercomputer system at the Advanced Fluid Information Research Center, Institute of Fluid Science, Tohoku University.

## Appendix A: SMAC method, convergence criteria and the divergenceless condition

In this Appendix A, we show how to obtain the solution  $\vec{V}(t)$  in Eq. (3) under the condition  $\partial\vec{V}/\partial t=0$  in Eq. (2). The relationship between Gaussian random number  $\vec{g}$  and Brownian force  $\vec{\eta}$  is given by  $\sqrt{2D\Delta t}\vec{g}=\vec{\eta}\Delta t$  [25]. Note that the discrete time  $t$  in Eq. (3) is introduced to obtain the steady-state solution that satisfies Eq. (2) and is different from the real time  $t$  in Eq. (1). This time can be called "fictitious time" because the divergenceless condition of Eq. (2) is not always satisfied until a convergent solution corresponding to the random force  $\sqrt{2D/\Delta t}\vec{g}$  is obtained. Thus, the Brownian random force  $\vec{g}$  is incremented only when the convergent solution  $\vec{V}$  of Eq. (3) is obtained. From Eq. (3), we understand that  $\nabla \cdot \vec{V}(t + \Delta t) = 0$  is not always satisfied even if  $\nabla \cdot \vec{V}(t) = 0$  is satisfied because the terms independent of  $\vec{V}(t)$  on the right-hand side are not always divergenceless. Moreover, the time evolution of  $p(t)$  is not specified. Therefore, we introduce a temporal velocity  $\vec{V}^*(t)$  and rewrite Eq. (3) as follows:

$$\vec{V}^*(t) = \vec{V}(t) + \Delta t \left[ \left( -\vec{V} \cdot \nabla \right) \vec{V}(t) - \rho^{-1} \nabla p(t) + \nu \Delta \vec{V}(t) \right] + \sqrt{2D\Delta t} \vec{g}(t), \quad (\text{A1})$$

$$\vec{V}(t + \Delta t) = \vec{V}^*(t) - \Delta t \rho^{-1} \nabla [p(t + \Delta t) - p(t)]. \quad (\text{A2})$$

By applying the divergence operator  $\nabla \cdot$  to Eq. (A2), we obtain

$$\nabla \cdot \vec{V}(t + \Delta t) = \nabla \cdot \vec{V}^*(t) - \Delta t \rho^{-1} \Delta [p(t + \Delta t) - p(t)]. \quad (\text{A3})$$

Then, assuming the condition  $\nabla \cdot \vec{V}(t + \Delta t) = 0$ , we obtain Poisson's equation for  $\phi(t) = p(t + \Delta t) - p(t)$ :

$$\Delta \phi(t) = \frac{\rho}{\Delta t} \nabla \cdot \vec{V}^*(t), \quad \phi(t) = p(t + \Delta t) - p(t). \quad (\text{A4})$$

Thus, combining Eq. (A1) for the time evolution of  $\vec{V}^*(t)$  with Poisson's equation in Eq. (A4) for  $\phi(t) = p(t + \Delta t) - p(t)$ , we implicitly obtain the time evolution  $\vec{V}(t + \Delta t)$  with the condition  $\nabla \cdot \vec{V}(t + \Delta t) = 0$ . The time evolution of  $p$  from  $p(t)$  to  $p(t + \Delta t)$  can also be obtained by adding the solution  $\phi(t)$  to  $p(t)$ , i.e.,  $p(t) + \phi(t)$ .

The simulation procedure can be summarized as follows:

- (i) Calculate  $V^*(t)$  by Eq. (A1) using the current  $V(t)$ ,  $p(t)$  and  $\vec{g}$
- (ii) Solve Poisson's equation for  $\phi(t)$  in Eq. (A4)
- (iii) Calculate  $V(t + \Delta t)$  and  $p(t + \Delta t)$  by Eq. (A2) and  $p(t) + \phi(t)$ , respectively
- (iv) Repeat steps (i)–(iii) until the convergence criteria given below are satisfied

This technique for updating  $\vec{V}(t)$  is slightly different from that of the original MAC method, where  $\vec{V}(t)$  is explicitly updated to  $\vec{V}(t + \Delta t)$ ; hence,  $\nabla \cdot \vec{V} = 0$  is not always satisfied and may be slightly violated even for the convergent solution. This violation becomes larger for larger Brownian force strength  $D$  in the original MAC method; however, it is negligibly small for the convergent solutions in the SMAC method. Detailed information on  $\nabla \cdot \vec{V} = 0$  is given below. The most time-consuming part of this process is to solve the Poisson equation for  $\phi$ , which is simulated by the Open-Mp parallelization technique coded in Fortran.

We assume the following convergence criteria for  $\vec{V}$  and  $p$ :

$$\begin{aligned}
& \text{Max} \left[ \left| |\nabla \cdot \vec{V}_{ijk}(t + \Delta t)| - |\nabla \cdot \vec{V}_{ijk}(t)| \right| \right] < 1 \times 10^{-8}, \\
& \text{Max} \left[ |\vec{V}_{ijk}(t + \Delta t) - \vec{V}_{ijk}(t)| \right] < 1 \times 10^{-8}, \\
& \text{Max} [|p_{ijk}(t + \Delta t) - p_{ijk}(t)|] < 1 \times 10^{-8},
\end{aligned} \tag{A5}$$

and the criterion for the Poisson equation iterations is

$$\text{Max} [|\phi_{ijk}(n + 1) - \phi_{ijk}(n)|] < 1 \times 10^{-10}, \tag{A6}$$

where  $n$  denotes the iteration step for solving the Poisson equation in Eq. (A4). Note that the first condition in Eq. (A5) is satisfied in the early iterations; therefore, this convergence condition is actually unnecessary. One additional point to note is that only the convergent solution satisfies  $\nabla \cdot \vec{V} = 0$ . In this sense, the obtained numerical solution of the LNS equation in Eq. (1) is a steady-state solution characterized by Eq. (2).

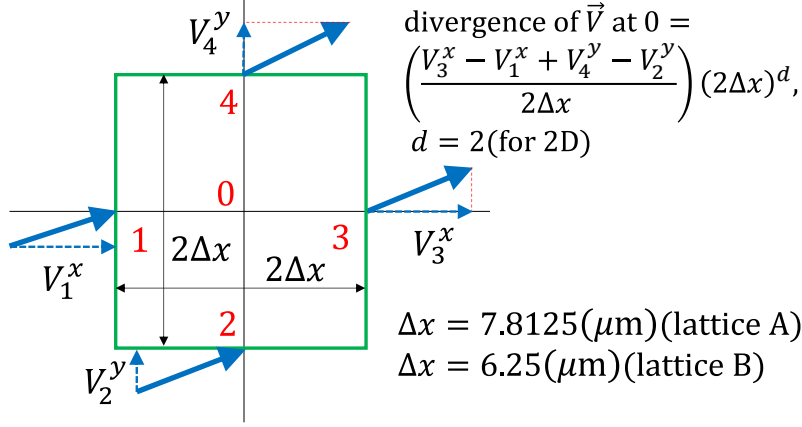


FIG. 17. Illustration of the divergence  $(2\Delta x)^2 \nabla \cdot \vec{V}$  at lattice point 0, where the dimension is assumed to be  $D = 2$  for simplicity and where the lattice spacing  $\Delta x$  is assumed in the 3D simulations on lattice A and lattice B in this paper.

To check the accuracy of this technique, we calculate the lattice average  $\text{Div}_{\text{ab}}$  of  $|\nabla \cdot \vec{V}|$ :  $\text{Div}_{\text{ab}} = (2\Delta x)^3 \sum_{ijk} |\nabla \cdot \vec{V}_{ijk}| / \sum_{ijk} 1 (\text{m}^3/\text{s})$ , where  $\sum_{ijk} 1$  is the total number of internal lattice points and where  $\nabla \cdot \vec{V}_{ijk} = (V_{i+1jk}^x - V_{i-1jk}^x + V_{ij+1k}^y - V_{ij-1k}^y + V_{ijk+1}^z - V_{ijk-1}^z) / (2\Delta x)$ . Here,  $\text{Div}_{\text{ab}}$  is considered to be the lattice average of the fluid volume flowing into or out of a cubic lattice enclosing a lattice point per second according to the Gauss theorem (see Fig. 17 for the 2D case). For  $D = 0$ , we numerically obtain  $\sum_{ijk} |\nabla \cdot \vec{V}_{ijk}| = 0 (1/\beta\text{s})$  for every time step  $t$  (see Appendix B for the simulation unit  $\beta$ ); hence,  $\text{Div}_{\text{ab}} = 0$  for all lattice points, which implies that  $\nabla \cdot \vec{V} = 0$  on lattice B. We also have  $\sum_{ijk} |\nabla \cdot \vec{V}_{ijk}| \simeq 7.9 \times 10^{-9} (1/\beta\text{s}) = 1.9 \times 10^{-7} (1/\text{s})$  on lattice A, which implies that the total divergence is given by  $(2\Delta x)^3 \sum_{ijk} |\nabla \cdot \vec{V}_{ijk}| \simeq 7.4 \times 10^{-4} (\mu\text{m}^3/\text{s}) = 7.4 \times 10^{-10} (\mu\text{g}/\text{s})$ , where  $\Delta x = 7.8125 (\mu\text{m})$ , and  $1 (\mu\text{m}^3)$  is replaced by  $10^{-6} (\mu\text{g})$  because the density  $\rho$  is considered to be the same as that of water  $\rho = 10^3 (\text{kg}/\text{m}^3) = 10^{-3} (\text{g}/\text{mm}^3) = 10^{-12} (\text{g}/\mu\text{m}^3)$ . This value of the total divergence  $7.4 \times 10^{-10} (\mu\text{g}/\text{s})$ , which implies  $\text{Div}_{\text{ab}} \simeq 6.5 \times 10^{-16} (\mu\text{g}/\text{s})$ , is sufficiently small for the scales of protoplasmic streaming, where  $\sum_{ijk} 1 = 1, 153, 800$  is used for the total number of internal points of lattice A. Detailed information on the lattice geometry is presented in Section II B.

In the case of  $D \neq 0$ , the total divergence fluctuates from one convergent configuration to another depending on the Brownian random forces. However, its mean value is almost independent of  $D$ , and the maximum value is approximately given by  $\sum_{ijk} |\nabla \cdot \vec{V}_{ijk}| = 1 \times 10^{-7} (1/\beta\text{s})$ , which is independent of lattices A and B; this value is comparable to the

abovementioned value for  $D = 0$  on lattice A. Thus, we find that the SMAC method is successful for the divergenceless condition in simulating the 3D LNS equation in Eq. (1) under the condition of Eq. (2).

## Appendix B: Physical units and simulation units

In the simulations, the physical units (m, s, kg) are changed to simulation units ( $\alpha\text{m}$ ,  $\beta\text{s}$ ,  $\lambda\text{kg}$ ) using positive numbers  $\alpha$ ,  $\beta$  and  $\lambda$ . Using these numbers for  $V_e$ ,  $\nu_e$ , and  $\rho_e$ , we have the relations  $V_e[\text{m/s}] = V_e\beta/\alpha[\alpha\text{m}/(\beta\text{s})]$ ,  $\nu_e[\text{m}^2/\text{s}] = \nu_e\beta/\alpha^2[(\alpha\text{m})^2/(\beta\text{s})]$ , and  $\rho_e[\text{kg}/\text{m}^3] = \rho_e\alpha^3/\lambda[\lambda\text{kg}/(\alpha\text{m})^3]$  in physical units. The right-hand sides of these relations can be written as  $V_0[\alpha\text{m}/(\beta\text{s})]$ ,  $\nu_0[(\alpha\text{m})^2/(\beta\text{s})]$ , and  $\rho_0[\lambda\text{kg}/(\alpha\text{m})^3]$  in the simulation units. Therefore,

$$\alpha = \frac{\nu_e V_0}{\nu_0 V_e}, \quad \beta = \frac{\nu_e}{\nu_0} \left( \frac{V_0}{V_e} \right)^2, \quad \lambda = \frac{\rho_e}{\rho_0} \left( \frac{\nu_e V_0}{\nu_0 V_e} \right)^3. \quad (\text{B1})$$

In addition to these numbers, we need positive numbers  $\gamma$  and  $\delta$  for the lattice and time discretization such that  $n_X \rightarrow \gamma n_X$  and  $n_T \rightarrow \delta n_T$  for the physical quantities to be independent of  $n_X$  and  $n_T$ . In this expression,  $n_X$  and  $n_T$  are connected to the lattice spacing  $\Delta x(\text{m})$  and discrete time step  $\Delta t(\text{s})$ , respectively, such that  $\Delta x(\text{m}) = d_e/n_X$  and  $\Delta t(\text{s}) = \tau_e/n_T$ , where  $\tau_e$  is the relaxation time [56, 57]. In this paper, we do not provide details on this problem for  $n_X$  and  $n_T$ , and  $\gamma$  and  $\delta$  are fixed to  $\gamma = 1$  and  $\delta = 1$ . This problem is studied in Ref. [26], where the  $\Delta t$  dependence is studied under  $\gamma = 1$ .

We assume the values given in Table VI for the unit change. Using the assumed numbers

TABLE VI. Values for the change of physical units and simulation units.

| $\alpha$           | $\beta$            | $\lambda$           | $\gamma$ | $\delta$ |
|--------------------|--------------------|---------------------|----------|----------|
| $2 \times 10^{-6}$ | $4 \times 10^{-2}$ | $8 \times 10^{-12}$ | 1        | 1        |

$\alpha$ ,  $\beta$ , and  $\gamma$  in Table VI, we have  $V_0 = V_e\beta/\alpha = (50 \times 10^{-6})(4 \times 10^{-2})/(2 \times 10^{-6}) = 1[\alpha\text{m}/(\beta\text{s})]$ ,  $\nu_0 = \nu_e\beta/\alpha^2 = (1 \times 10^{-4})(4 \times 10^{-2})/(2 \times 10^{-6})^2 = 1 \times 10^{-6}[(\alpha\text{m})^2/(\beta\text{s})]$ , and  $\rho_0 = \rho_e\alpha^3/\lambda = (1 \times 10^3)(2 \times 10^{-6})^3/(8 \times 10^{-12}) = 1 \times 10^{-3}[\lambda\text{kg}/(\alpha\text{m})^3]$ .

The strength of the random force  $D_e(\text{m}^2/\text{s}^3)$  is expressed by  $D((\alpha\text{m})^2/(\beta\text{s})^3)$  in the

simulation units such that

$$\begin{aligned}
D_e(\text{m}^2/\text{s}^3) &= \alpha^{-2}\beta^3 D_e((\alpha\text{m})^2/(\beta\text{s})^3) = 1.6 \times 10^5 D_e((\alpha\text{m})^2/(\beta\text{s})^3), \\
\Leftrightarrow D &= \alpha^{-2}\beta^3 D_e = 1.6 \times 10^5 D_e((\alpha\text{m})^2/(\beta\text{s})^3) \\
\Leftrightarrow D_e &= 6.25 \times 10^{-6} D(\text{m}^2/\text{s}^3).
\end{aligned} \tag{B2}$$

In the simulations,  $D(= 1.6 \times 10^5 D_e)((\alpha\text{m})^2/(\beta\text{s})^3)$  is varied implying that  $D_e(\text{m}^2/\text{s}^3)$  is varied.

The lattice spacing  $\Delta x_0$  in the simulation units is given by  $\Delta x_0 = \alpha^{-1} \frac{d_e}{n_X} = (2 \times 10^{-6})^{-1} (500 \times 10^{-6}) / (2R)$ , where the diameter  $2R$  of the cylinder is assumed to be  $n_X$ , which is the total number of discretizations introduced for a regular square lattice of size  $L \times L$  with  $L = n_X \Delta x_0$ . For  $n_X = 2R = 64$  on lattice A ( $n_X = 2R = 80$  on lattice B), we have  $\Delta x_0 = 3.90625$  ( $\Delta x_0 = 3.125$ ) in the simulation unit ( $\alpha\text{m}$ ) and  $\Delta x_0 = 7.8125$  ( $\Delta x_0 = 6.25$ ) in the physical unit ( $\mu\text{m}$ ).

The discrete time step  $\Delta t_0$  can also be expressed by  $\Delta t_0 = \beta^{-1} \frac{\tau_e}{n_T}$  using the macroscopic relaxation time  $\tau_e$  and total number of time discretizations  $n_T$ . However,  $\tau_e$  is not always given, so we simply assume  $\Delta t_0 = 5 \times 10^{-7}$  in the simulation unit ( $\beta\text{s}$ ) and  $\Delta t_0 = 2 \times 10^{-2}$  in the physical unit ( $\mu\text{s}$ ).

### Appendix C: Calculation technique for the velocity distribution

In this Appendix, we show the calculation technique for the velocity distribution  $h(V)$  in detail. The same technique is applied to  $h(V_z)$  by replacing  $V \rightarrow |V_z|$ , where  $h(V_z) = h(-V_z)$  is assumed due to the symmetric flow along the  $z$  axis in the simulations. The total number of cross sections are 360 in lattice A and 80 in lattice B, and the total number of sample configurations are 100 for lattices A and B, which are smaller than 1000 for the calculation of  $V_z(r, \theta)$  at three different  $\theta$ . However,  $h(V)$  and  $h(V_z)$  are calculated on all cross sections, and hence, the statistics is relatively high compared with the case of  $V_z(r, \theta)$ , which is calculated only on the cross section at  $z = L/2$ . We should note that the velocities of the boundary points are not included in the sample configurations.

To calculate the distribution  $h(V)$ , we first search the maximum velocity  $V^{\max}$  in the whole sample configurations of each value of  $D$  and define the width of velocity by  $\Delta V = V^{\max}/n$ , where  $n = 100$  for lattices A and B (Fig. 18). The histogram  $h(V_i)$ , ( $0 \leq i \leq n$ ) at  $V_i = i\Delta V$  is calculated by counting the number of lattice sites where the velocity  $V$  satisfies



discretization using Gaussian random numbers  $\vec{g}_{ijk}$  with mean 0 and variance 1 as described in Appendix A. Thus, we arrive at the discrete LNS equation in Eq. (3). The convergent solution  $\vec{V}_{ijk}(t)$  with impulse  $\vec{H}_{ijk}(t; \Delta t)$  is numerically obtained with the fictitious time evolution as described in Appendix A.

## Appendix E: Size of the fluid lump

The Maxwell-Boltzmann distribution of the velocity distribution is described by  $f(V) \propto V^2 \exp(-\frac{mV^2}{2k_B T})$ , where  $m$  is mass of thermally fluctuating particles. From this expression, we obtain the peak position of  $u^{\text{MB}}$  such that

$$u^{\text{MB}} = \sqrt{\frac{2k_B T}{m}}. \quad (\text{E1})$$

This expression give us a rough estimate of  $m$  such that  $m = 2k_B T / (u^{\text{MB}})^2$ . We assume that  $m \simeq \rho(d_{\text{fluid}})^3$ , where  $d_{\text{fluid}}$  is the size of fluid particle and  $\rho = 10^3(\text{kg/m}^3)$  is the density of water, then we have  $d_{\text{fluid}} \simeq [2k_B T / ((u^{\text{MB}})^2 \rho)]^{1/3}(\text{m})$ . By using  $k_B T \simeq 4 \times 10^{-21}(\text{m}^2 \text{kg/s}^2)$  for the room temperature  $T = 300(\text{K})$ , and the assumed value of  $c = 0.2$  in Eq. (8) for example, we have  $u^{\text{MB}} = 0.2 \times 43 = 8.6(\mu\text{m/s})$  and obtain  $d_{\text{fluid}} \simeq 48(\mu\text{m})$ .

The polynomial function  $h_0(u)$  of Eq. (8) corresponding to  $h(V_z)$  at  $D=0$  of lattice A in Fig. 6(a) is given by

$$h_0(u) = \begin{cases} \sum_{i=0}^8 a_i u^i, & (1 \geq u \geq 0) \\ \sum_{i=0}^8 a_i (-u)^i & (-1 \leq u < 0) \end{cases},$$

$$a_0 = 3.25 \times 10^{-1}, a_1 = 1.25 \times 10^{-1}, a_2 = -1.78,$$

$$a_3 = 1.49 \times 10^1, a_4 = -5.58 \times 10^1, a_5 = 1.18 \times 10^2,$$

$$a_6 = -1.40 \times 10^2, a_7 = 8.79 \times 10^1, a_8 = -2.24 \times 10^1.$$
(E2)

## REFERENCES

- 
- [1] J. Verchot-Lubicz, and R.E.Goldstein, *Cytoplasmic streaming enables the distribution of molecules and vesicles in large plant cells*, *Protoplasma*, **240**, 99-107.(2009); DOI 10.1007/s00709-009-0088-x

- [2] T. Shimmen and T. Yokota, *Cytoplasmic streaming in plants*, Current Opinion in Cell Biology, **16** (1), 68–72 (2004); <https://doi.org/10.1016/j.ceb.2003.11.009>
- [3] M. Tominaga and K. Ito, *The molecular mechanism and physiological role of cytoplasmic streaming*, Current Opinion in Plant Biology, **27**, 104–110 (2015); <https://doi.org/10.1016/j.pbi.2015.06.017>
- [4] T.M. Squires and S.R. Quake, *Microfluidics: Fluid physics at the nanoliter scale.*, Rev. Mod. Phys. **77**, 977–1026 (2005); <https://doi.org/10.1103/RevModPhys.77.977>
- [5] B.B. McIntosh and E.M. Ostap, *Myosin-I molecular motors at a glance*, Cell Science at a Glance, **129**, 2689–2695 (2016); <https://doi.org/10.1242/jcs.186403>
- [6] R.D. Astumian, *Thermodynamics and Kinetics of a Brownian Motor*, Science, **276**, 917–922 (2020); <http://science.sciencemag.org/content/276/5314/917>
- [7] F. Jülicher, A. Ajdari and J. Prost, *Modeling molecular motors*, Rev. Mod. Phys. **69**(4), 1269–1282 (1997); <https://link.aps.org/doi/10.1103/RevModPhys.69.1269>
- [8] J-W. Meent, I. Tuvalk and R.E. Goldstein, *Nature’s Microfluidic Transporter: Rotational Cytoplasmic Streaming at High Péclet Numbers*, Phys. Rev. Lett. **101**, 178102(1-4) (2008); DOI: 10.1103/PhysRevLett.101.178102
- [9] R.E. Goldstein, I. Tuvalk and J-W. van de Meent, *Microfluidics of cytoplasmic streaming and its implications for intracellular transport*, PNAS, **105**, 3663-3667 (2008); <https://www.pnas.org/cgi/doi/10.1073/pnas.0707223105>
- [10] J-W. van De Meent, A.J. Sederman, L.F. Gladden and R.E. Goldstein, *Measurement of cytoplasmic streaming in single plant cells by magnetic resonance velocimetry*, J. Fluid Mech. **642**, pp.5-14 (2010); doi:10.1017/S0022112009992187
- [11] R.E. Goldstein and J-W. van de Meent, *Physical perspective on cytoplasmic streaming*, Interface Focus. **5**: 20150030; <https://doi.org/10.1098/rsfs.2015.0030>
- [12] K. Kikuchi and O. Mochizuki, *Diffusive Promotion by Velocity Gradient of Cytoplasmic Streaming (CPS) in Nitella Internodal Cells*, Plos One, 0144938(1-12) (2015); <https://DOI:10.1371/journal.pone.0144938>
- [13] R. Niwayama, K. Shinohara and A. Kimura, *Hydrodynamic property of the cytoplasm is sufficient to mediate cytoplasmic streaming in the Caenorhabditis elegans embryo*, PNAS, vol. **108**, pp.11900-11905 (2011); <https://doi.org/10.1073/pnas.1101853108>
- [14] N. Kamiya and K. Kuroda, *Velocity Distribution of the Protoplasmic Streaming in Nitella*



- Cells*, Bot, Mag. Tokyo, **69**, 544-554 (1956); <https://doi.org/10.15281/jplantres1887.69.544>,
- [15] N. Kamiya and K. Kuroda, *Measurement of the Motive Force of the Protoplasmic Rotation in Nitella*, Protoplasma, **50**, 144-147 (1958).
- [16] N. Kamiya and K. Kuroda, *Dynamics of Cytoplasmic Streaming in a Plant Cell*, Biorheology, **10**, 179-187 (1973).
- [17] N. Kamiya, *Cytoplasmic streaming in giant algal cells: A historical survey of experimental approaches*, Bot, Mag. Tokyo, **99**, 441-496 (1986); <https://doi.org/10.1007/BF02488723>
- [18] M. Tazawa, *Motive force of the cytoplasmic streaming in Nitella*, Protoplasma, **65**, 207-222 (1968).
- [19] W. F. Pickard, *Further observations on cytoplasmic streaming in Chara braunii*, Can. J. Bot. **50**, 703-711 (1971).
- [20] A private communication of the author H.K. with Dr. Kazuhiko Mitsuhashi, who obtained *Nitella axilliformis Imahori* delivered by the Microbial Culture Collection at the National Institute for Environmental Studies, Japan.
- [21] R.V. Mustacich and B.R. Ware, *Observation of Protoplasmic Streaming by Laser-Light Scattering*, Phys. Rev. Lett. **33**, 617-620 (1974).
- [22] R.V. Mustacich and B.R. Ware, *A Study of Protoplasmic Streaming in Nitella by Laser Doppler spectroscopy*, Biophys. J. **16**, 373-388 (1976).
- [23] R.V. Mustacich and B.R. Ware, *Velocity Distributions of the Streaming Protoplasm in Nitella Flexilis*, Biophys. J. **17**, 229-241 (1977).
- [24] D.B. Sattelle and P.B. Buchan, *Cytoplasmic Streaming in Chara Corallina studied by Laser Light Scattering*, J. Cell. Sci. **22**, 633-643 (1976).
- [25] V. Egorov O. Maksimova, I. Andreeva, H.Koibuchi, S. Hongo, S. Nagahiro, H. Ikai, M. Nakayama, S. Noro, T. Uchimoto and J-P. Rieu, *Stochastic fluid dynamics simulations of the velocity distribution in protoplasmic streaming*, Phys. Fluids, **32**, 121902(1-15) (2020); <https://doi.org/10.1063/5.0019225>
- [26] S. Noro, S. Hongo, S. Nagahiro, H. Ikai, H. Koibuchi, M. Nakayama, T. Uchimoto and J-P. Rieu, *Langevin Navier-Stokes simulation of protoplasmic streaming by 2D MAC method*, ArXiv 2112.10901.
- [27] M.T. Hossain, I.D. Gates and G. Natale, *Dynamics of Brownian Janus rods at a liquid-liquid interface*, Phys. Fluids **34**, 012117 (2022); <https://doi.org/10.1063/5.0076148>.

- [28] L.D. Landau and E.M. Lifschitz, *Course of Theoretical Physics*, Vol. 9, Statistical Physics, Part 2, Chapter IX, Hydrodynamic Fluctuations.
- [29] D. L. Ermak and J. A. McCammon, *Brownian dynamics with hydrodynamic interactions*, J. Chem. Phys. **69**, 1352 (1978); <https://doi.org/10.1063/1.436761>.
- [30] J. F. Brady and G. Bossis, *Stokesian Dynamics*, Ann. Rev. Fluid Mech. **20**, pp. 111-57 (1988); <https://doi.org/10.1146/annurev.fl.20.010188.000551>.
- [31] J. N. Roux, *Brownian particles at different times scales: a new derivation of the Smoluchowski equation*, Physica A **188**, pp. 526-552, (1992); [https://doi.org/10.1016/0378-4371\(92\)90330-S](https://doi.org/10.1016/0378-4371(92)90330-S).
- [32] P. J. Hoogerbrugge and J. M. Kolesman, *Simulating Microscopic Hydrodynamic Phenomena with Dissipative Particle Dynamics*, Europhys. Lett., **19** (3), pp. 155-160 (1992); DOI 10.1209/0295-5075/19/3/001.
- [33] P. Español and P. Warren, *Statistical Mechanics of Dissipative Particle Dynamics*, Europhys. Lett., **30** (4), pp. 191-196 (1995); DOI 10.1209/0295-5075/30/4/001.
- [34] P. Español, *Dissipative particle dynamics with energy conservation*, Europhys. Lett., **40** (6), pp. 631-636 (1997); DOI 10.1209/epl/i1997-00515-8.
- [35] C. S. Peskin, *The immersed boundary method*, Acta Numerica, pp. 479-517 (2002); DOI 10.1017/S0962492902000077.
- [36] P. R. Kramer and A. J. Majda, *Stochastic Mode Reduction for the Immersed Boundary Method*, SIAM J. Appl. Math. **64**, No. 2, pp. 369-400 (2004); <https://doi.org/10.1137/S003613990342213>.
- [37] P. R. Kramer, C. S. Peskin and P. J. Atzberger, *On the foundations of the stochastic immersed boundary method*, Computer Methods in Applied Mechanics and Engineering, **197**, Issues 25-28, pp. 2232-2249 (2008); <https://doi.org/10.1016/j.cma.2007.11.010>.
- [38] S. Succi, *The Lattice Boltzmann Equation: For Fluid Dynamics and Beyond (Numerical Mathematics and Scientific Computation)*, (Clarendon Press, Oxford, 2001).
- [39] A.J.C. Ladd, *Short-Time Motion of Colloidal Particles: Numerical Simulation via a Fluctuating Lattice-Boltzmann Equation*, Phys. Rev. Lett. **70**, 1339-1342 (1993).
- [40] A. Bhaduria, B. Dorschner, and I. Karlin, *Lattice Boltzmann method for fluid-structure interaction in compressible flow*, Phys. Fluids **33**, 106111 (2021); <https://doi.org/10.1063/5.0062117>.
- [41] X. Fu, J. Sun, and Y. Ba, *Numerical study of droplet thermocapillary migration behavior on*

- wettability-confined tracks using a three-dimensional color-gradient lattice Boltzmann model*, Phys. Fluids **34**, 012119 (2022); <https://doi.org/10.1063/5.0078345>.
- [42] T. Inamuro, M. Yoshino, and F. Ogino, *Accuracy of the lattice Boltzmann method for small Knudsen number with finite Reynolds number*, Phys. Fluids **9**, 3535 (1997); <https://doi.org/10.1063/1.869426>.
- [43] G.G. Batrouni, G.R. Katz, A.S. Kronfeld, G.P. Lepage, B.Svetitsky and K.G. Wilson, *Langevin simulations of lattice field theories*, Phys. Rev. D **32** 2736-2747 (1985).
- [44] A. Ukawa and M. Fukugita, *Langevin Simulation Including Dynamical Quark Loops*, Phys. Rev. Lett. **55**, 1854-1857 (1985).
- [45] K. Höfler and S. Schwarzer, *Navier-Stokes simulation with constraint forces: Finite-difference method for particle-laden flows and complex geometries*, Phys. Rev. E. **61**, 7146-7160 (2000).
- [46] M. I. Kopp and V. V. Yanovsky, *Influence of the Hall current on the convective and magnetorotational instability in a thin layer of an electrically conductive nanofluid*, Phys. Fluids **34**, 064107 (2022); <https://doi.org/10.1063/5.0094977>.
- [47] McKee S, Tomé MF, Ferreira VG, Cuminato JA, Castelo A, Sousa FS, Mangiavacchi N. The MAC method. Computers & Fluids 2008;37: 907-930. doi:10.1016/j.compfluid.2007.10.006
- [48] M. Doi, Soft matter physics (Oxford University Press, 2013).
- [49] Doi, M.; Edwards, S.F. *The Theory of Polymer Dynamics*; Oxford University Press: Oxford, UK, 1986.
- [50] Y. Kantor and D.R. Nelson, Phys. Rev. A **36**, 4020 (1987).
- [51] Nelson, D. The Statistical Mechanics of Membranes and Interfaces. In *Statistical Mechanics of Membranes and Surfaces*, 2nd ed.; Nelson, D., Piran, T., Weinberg, S., Eds.; World Scientific: Singapore, 2004; pp. 1–17.
- [52] M. Creutz, *Quarks, gluons and lattices*, (Cambridge University Press, Cambridge, 1983.
- [53] N. Metropolis, A.W. Rosenbluth, M.N. Rosenbluth, A.H.Teller, Equation of State Calculations by Fast Computing Machines. *J. Chem. Phys.* **1953**, *21*, 1087–1092.
- [54] D.P. Landau, Finite-size behavior of the Ising square lattice. *Phys. Rev. B.* **1976**, *13*, 2997–3011.
- [55] A. Passos, J. M. Sherwood, E. Kaliviotis, R. Agrawal, C. Pavesio, and S. Balabani, *The effect of deformability on the microscale flow behavior of red blood cell suspensions*, Phys. Fluids **31**, 091903 (2019); <https://doi.org/10.1063/1.5111189>.

- [56] W.T. Coffey and Yu.P. Kalmykov, *On the calculation of the macroscopic relaxation time from the Langevin equation for a dipole in a cavity in a dielectric medium*, Chemical Physics **169**, pp.165-172 (1993); [https://doi.org/10.1016/0301-0104\(93\)80074-J](https://doi.org/10.1016/0301-0104(93)80074-J)
- [57] Y. Feldman, A. Puenko and Y. Ryabov, *Dielectric Relaxation Phenomena in Complex Materials*, in *Fractals, Diffusion, and Relaxation in Disordered Complex Systems*, Eds. W.T.Coffey and Y.P.Kalmykov, Advanced Chemical Physics Vol.133, Wiley-Interscience, New Jersey, 2006.